# Evolution and Geometry of Hot Spots in Supernova Remnant $1987A^1$

Ben E. K. Sugerman<sup>2</sup>

Department of Astronomy, Columbia University, New York, NY 10027

ben@astro.columbia.edu

Stephen S. Lawrence

Department of Physics, Hofstra University, Hempstead, NY 11549

 ${\tt Stephen.S.Lawrence@hofstra.edu}$ 

Arlin P. S. Crotts

Department of Astronomy, Columbia University, New York, NY 10027

arlin@astro.columbia.edu

and

Patrice Bouchet, and Steve R. Heathcote

Cerro Tololo Inter-American Observatory, Casilla 603, La Serena, Chile

pbouchet@noao.edu, sheathcote@noao.edu

## **ABSTRACT**

We present ground-based near-infrared imaging and HST optical imaging and spectroscopy of the interaction between the ejecta of SN 1987A and its equatorial circumstellar ring. This interaction has made a transition, from emission originating in just a few "hot spots" at restricted locations in position angle around the ring, to a collision producing optical emission over a nearly continuous distribution, with few breaks larger than 45 degrees. The centroids of the first three spots are measured to move at  $2000-3000~{\rm km~s^{-1}}$ , which we interpret as a lower limit of the velocity of the forward blast front. Multi-wavelength light curves of

the spots show that they do not evolve uniformly, and change significantly on timescales as short as one month; in particular the first spot shows a significant break in its lightcurve. Implications of observed delays between spots appearances are discussed, which leads to a generalized model of hot spot evolution, and suggests that the early appearance of the first hot spot is explained by its inward radial position and a fairly uniform forward blast wave, rather than extraordinary physical circumstances. Data further suggest that the forward blast is reaching the bulk of the inner ring material to the east, the density of which appears higher than elsewhere in the ring. We study the ring geometry, finding evidence suggestive of an intrinsic ellipticity of 0.95, and find lower and upper distance limits of  $47.9 \pm 0.92$  kpc and  $54.4 \pm 2.1$  kpc, respectively.

Subject headings: circumstellar matter — supernovae:individual (SNR 1987A) — supernova remnants

#### 1. INTRODUCTION

Supernova (SN) 1987A in the Large Magellanic Cloud is the first naked-eye SN in over three centuries, and the first SN remnant (SNR) seen to form within a pre-existing circumstellar environment that has been mapped in significant detail. It serves as a vital test bed for the colliding winds model of mass-loss nebulae and the interaction of SN ejecta with interstellar and circumstellar material (CSM); an important rung in the cosmological distance ladder; a valuable probe of the interstellar medium (ISM); and a unique laboratory for studying SNR formation and the final stages of massive star evolution.

Narrow emission lines in International Ultraviolet Explorer (IUE) spectra at day 80 (after SN) indicated the existence of a circumstellar nebula (Fransson et al. 1989) which was confirmed in long-slit [O III] and H $\alpha$  spectroscopy on day 300 by Wampler & Richichi (1989). The first resolved images were taken in these same bands by Crotts, Kunkel & McCarthy (1989) on day 750, and by Wampler et al. (1990) on day 1037, and indicated the existence of an elliptical structure with a central cavity, the latter evidenced by the rapid fall of radio signal from ejecta—CSM interaction shortly after the SN was discovered (Turtle et al.

<sup>&</sup>lt;sup>1</sup>Based in part on observations made with the NASA/ESA *Hubble Space Telescope*, obtained from the Data Archive at the Space Telescope Science Institute, which is operated by the Association of Universities for Research in Astronomy, Inc., under NASA contract NAS 5-26555.

 $<sup>^2\</sup>mathrm{Guest}$ observer, Cerro Tololo Inter-American Observatory

1987). Hubble Space Telescope (HST) imaging (Jakobsen et al. 1991; Jakobsen, Macchetto & Panagia 1993; Jakobsen et al. 1994; Plait et al. 1995; Burrows et al. 1995) revealed this structure to be a dense circumstellar equatorial ring (ER) flanked by two larger outer rings, while kinematics of the ER proved it to be a planar ring, expanding at  $\sim 10.3$  km s<sup>-1</sup> and inclined at  $\sim 43^{\circ}$ , rather than a limb-brightened ellipsoid (Crotts & Heathcote 1991).

In his model of self-similar interaction of ejecta with ambient media, Chevalier (1982) demonstrated the development of a double-shock system, in which a forward blast wave is driven into the CSM and a reverse shock is driven into the expanding ejecta, with a contact discontinuity between the shocked CSM and shocked ejecta. Models predicted this forward shock would impact the ER between 13–20 years after the SN explosion (Luo & McCray 1991; Luo, McCray & Slavin 1994; Chevalier & Dwarkadas 1995; Borkowski, Blondin & McCray 1997b). Making simple assumptions of symmetry, this impact was expected to appear as an initial brightening at the northern (closest) segment of the ER, and then spread in P.A. to engulf the entire ring within roughly 1 year, due to light-travel delays across the ER.

The first indications that the double-shock scenario was correct came in 1997 when a 250 km s<sup>-1</sup> blue-shifted H $\alpha$  feature was observed at P.A. 29° (Pun et al. 1997) and a Ly $\alpha$  feature was observed with velocity  $\lesssim 1.5 \times 10^4$  km s<sup>-1</sup> (Garnavich, Kirshner, & Challis 1997b) using the Space Telescope Imaging Spectrograph (STIS) aboard HST. This H $\alpha$  feature was quickly confirmed in Wide Field and Planetary Camera 2 (WFPC2) imaging (Garnavich, Kirshner, & Challis 1997a), and was interpreted as the first "hot spot" from the impact of high-velocity forward shock with the ER (Sonneborn et al. 1998). The Ly $\alpha$  feature has been modeled and interpreted as neutral hydrogen in the CSM between the SN and the ER crossing the reverse shock (Sonneborn et al. 1998; Michael et al. 1998, 1999; Michael 2000).

Contrary to the simplest expectations, no new loci of ER-ejecta interaction were discovered following the first hot spot for nearly three years, until Bouchet et al. (2000) reported a new brightening near P.A. 104° in ground-based He I imaging, which was soon followed by the discovery and confirmation of five additional spots in *HST* data (Lawrence & Crotts 2000; Maran, Pun, & Sonneborn 2000; Garnavich, Kirshner, & Challis 2000; Lawrence, Sugerman, & Crotts 2000; Lawrence et al. 2000, hereafter Paper I). In Paper I, we re-analyzed the WFPC2 data using PSF-matched difference imaging, and traced the appearance of the first hot spot (HS 1-029 using Paper I notation<sup>3</sup>) to 1995 March, as well as most of the newly-discovered spots to early 1999.

We are now observing a unique period in the formation of SNR 1987A as the high-

<sup>&</sup>lt;sup>3</sup>The first number represents the order of discovery, and the trailing three digits encode the first reported imaging P.A. of the feature

velocity SN debris overtakes the slowly expanding ER. While this interaction will eventually destroy the circumstellar nebula, it will provide unique opportunities in the coming years to explore the complicated products of stellar mass loss, by detailing the circumstellar environment directly through shock-heating. Furthermore, the X-ray and UV flux from this interaction will reionize unseen portions of the nebular structure, revealing many of them for the first time.

The visible consequences of the forward shock's impact on the ER are apparent and developing rapidly. In §2 we report new ground-based and STIS observations taken of SNR 1987A. Results are presented in §3. We show that between the years 2000 and 2001, the number of confirmed hot spots has nearly doubled (§3.1), with spots now located in a nearly continuous distribution about the ER (§3.2). We also show in §3.2 that the centroids of the first three hot spots display proper motion. We study the geometry of the ER in §3.3, which we use to build a deprojected view of the system in §3.4. Light curves for the hot spots are discussed in §3.5, and the bulk interaction between the ejecta and ER is examined in §3.6. In §4, we examine the accuracy of our detection and photometry methods. We discuss a general model for hot spot evolution in §5.1, and consider the implications of hot spot timing in §5.2, followed in §5.3 by a brief discussion regarding the distance to the SN.

### 2. OBSERVATIONS AND REDUCTIONS

We analyze data taken on the Cerro Tololo Inter-American Observatory (CTIO) 4-m telescope with tip-tilt first-order wavefront correction, as part of an ongoing ground-based monitoring campaign of the SN and its circumstellar environment. Data were taken on 2001 March 17–18 [3.7 hr total integration] and 2001 November 27–28 [1.5 hr total integration] with the OSIRIS imager in the He I 1.084 $\mu$ m line, and differenced from data reported in Paper I (1998 October 6 from CIRIM, 1.5 hr total integration; 1999 December 25 from OSIRIS, 3.5 hr total integration) using difimphot.

We analyze public and Director's Discretionary data from the HST archive, making use of:

- STIS spectra (G750M grating, 2"slit) from 1997 April 26 [day 3714], 2000 May 1 [day 4816], 2000 October 21 [day 4996] and 2001 April 27 [day 5176];
- STIS F28X50LP imaging taken between 1997 December and 2001 April [days 3941–5176]; and
- WFPC2 images taken through F336W, F439W, F555W, F656N, F658N, F675W, and

F814W between 1994 February and 2000 February [days 2537–4725].

For clarity, Figure 1 shows the correspondence between the number of days following the SN, the calendric date, and the epochs of all data mentioned above.

Pipeline reduced HST spectra and imaging were taken directly from the archive, and aberrant pixels (listed in the data quality and hot pixel files<sup>4</sup>) were fixed using the method to be described shortly. STIS spectra were co-added using cosmic-ray rejection, and finally wavelength calibrated using stsdas within the IRAF data reduction and analysis system<sup>5</sup>. Cleaned WFPC2 and STIS images were summed with cosmic-ray rejection, and Stars 2 and 3 were removed using Tiny Tim model point-spread functions (PSFs), and geometric distortions in the PC chip (Holtzman et al. 1995) were corrected using the drizzle routine with a 1:1 resampling. Images were finally unsharp masked to remove any sky background. As in Paper I, we apply the difimphot image subtraction techniques of Tomaney & Crotts (1996), which employ Fourier techniques to match empirically-derived stellar profiles between two images. This technique is limited to data with resolution better than  $\sim 2.2$  pixels per FWHM, an effective critical minimum required for Fourier transforms of imaging data (R. Uglesich, private communication). Since the PC and STIS images have a nominal resolution of  $\sim 1.7$ pixels, we convolve the data with a circular Gaussian of  $\sigma = 0.65$  to achieve a final stellar PSF of FWHM  $\gtrsim 2.3$  pixels. Data are finally geometrically registered to a common orientation with residuals  $\leq 0.05$  pixel rms (PC) and  $\leq 0.1$  pixel rms (STIS). Aperture and crowded-field photometry was performed using standard daophot (Stetson 1987) techniques with Tiny Tim model PSFs processed by identical procedures as the data to mimic the registration steps. PC fluxes were calculated using symphot, including decontamination corrections, while STIS imaging fluxes are presented in instrumental counts  $\sec^{-1}$ .

As briefly outlined in Paper I, hot pixels account for  $\sim 1\%$  of both the PC and STIS chips, and since most images were not spatially dithered, these pixels present a stochastic and non-Gaussian source of noise. During the reduction procedures (registration and smoothing), single hot pixels can take on point-source-like profiles, thereby creating a strong source of false signals. We correct known bad pixels by replacing each with the median value of the 8 surrounding pixels, taken from an initial cosmic-ray cleaned image. The difference between the original and cleaned images is a "contamination image," i.e. a map of the bad pixels locations, which accompanies each data image through each step of the reduction

<sup>&</sup>lt;sup>4</sup>available at http://www.stsci.edu/instruments/wfpc2/wfpc2\_hotpix.html

<sup>&</sup>lt;sup>5</sup>*IRAF* is distributed by the National Optical Astronomy Observatories, which are operated by the Association of Universities for Research in Astronomy, Inc., under cooperative agreement with the National Science Foundation.

pipeline. Since many data sets consist of only two images, often not spatially dithered, we recognize that this correction technique is predominantly cosmetic, and hence to minimize false detections in our analysis, a potential hot spot signal must not lie within a bad-pixel domain, and must appear in at least two difference images created from mutually exclusive epochs.

#### 3. RESULTS

# 3.1. Discovery of New Hot Spot Activity

As in Paper I, we perform difference-image analysis to search for new hot spots. The contrast between hot spots and the underlying ER is greater in He I  $1.083\mu$ m than in optical lines at early times (Paper I), thus He I imaging is a sensitive probe of new ER-ejecta interaction. Figure 2 displays a tiling of images from our ground-based monitoring. Panel (a) shows the ER and HS 1-029 resolved between Stars 2 and 3 on 1998 October 6, taken with the CIRIM imager. Panels (b)–(d) show data from the OSIRIS imager taken on 1999 December 25; 2001 March 17–18; and 2001 November 27–28 (as noted in each window). Panel (c) clearly shows the brightening of the spot 2–5 complex, and the fading of Star 3 (a known variable star). In panel (d), we see that hot spot flux has dramatically brightened in eight months, nearly engulfing the entire ER.

Panels (e)–(h) display PSF-matched difference images made with the above data, as noted in the top of each window. The discovery data from Bouchet et al. (2000) is shown in panel (e). This difference image, between 1998 and 1999, was photometrically scaled using the fluxes of stars of constant brightness located throughout the field. As such, white regions have brightened and black regions have faded since the earlier epoch. We see the continued brightening of HS 1-029, the faint appearance of HS 2-104, and the fading ER to the west. Panel (f) displays the data from 2001 March subtracted by 1999 December, again scaled photometrically to constant stellar flux. While hot spot emission from P.A. 30°-150° is clear, comparison of the western half of the ER to that in panel (e) reveals that the fading ER has been offset by a continuous locus of brightening flux. This trend is confirmed in panel (g), a difference image made between 2001 November and 1999 December, in which we now see the southwestern limb of the ER standing out distinctly from the background. To better examine the extent of this brightening, we display the difference between 2001 November and 2001 March in panel (h). Flux is evident along the entire ER except the region roughly located between P.A. 160° and P.A. 210°; even this latter region must be brightening marginally, otherwise the fading of the underlying ER would result in negative (black) pixels. At this resolution, we can not be certain of the actual distribution of sources producing this continuous, positive image superposed on the fading ER material. We consider it realistic that this reflects unresolved emission from a population of young hot spots distributed roughly uniformly about the ER. Flux has increased around the position of HS 1-029 the most, yet the flux distribution at this position is elongated (south and westward), notably differing from the image's PSF. This is suggestive that the brightening is not due to HS 1-029 alone, but can be attributed to the rapid brightening of a population of spots on either side of HS 1-029.

While the above ground-based data are effective at describing the global behavior of the ER-ejecta interaction, we study the smaller-scale evolution with *HST*. The ER is resolved well enough to allow us to compensate for its fading by scaling images to be differenced by its flux (rather than by constant stellar photometry), which we measure in elliptical arcs in both images. For most epochs, we employ an arc of radial width 0.66 between P.A. 300°–10°, however as more of the ER becomes contaminated with new spots, we co-add several smaller arcs distributed about the ring. Since the ER fades non-uniformly, the ring is often over-subtracted in some places, and stellar residuals often remain.

Figure 3a shows a difference image in F656N<sup>6</sup> between 2000 February 2 and 1998 February 5. The flux from HS 1-029 has been removed using the  $Tiny\ Tim$  model PSF, however a small core remains. We clearly see the first six spots, as reported from these data by Garnavich, Kirshner, & Challis (2000) using independent reduction techniques, as well as HS 7-289 reported by Lawrence, Sugerman, & Crotts (2000). A faint signature of HS 10-040, as well as marginal features at P.A. 174° and 314°, as reported by Sugerman, Lawrence & Crotts (2000) from 2000 May 1 STIS observations, are also detectable. Since stellar residuals remain due to the ER scaling, flux from HS 6-229 is a combination of emission from the hot spot and coincident Star 5 (P.A.=230°, r = 0.773).

In light of the rapid developments in hot spot discovery in early 2000, we took STIS spectra and imaging on 2000 May 1, 2000 October 29, and 2001 April 27 (through Director's Discretionary observing time on HST). Figure 3b shows a difference image made in the F28X50LP imaging filter, between 2000 November 3 and 1998 November 14. Again, flux from HS 1-029 has been removed. In addition to the aforementioned spots, HS 11-355 (Sugerman, Lawrence & Crotts 2000) can be seen. Figure 3c shows a similar difference image in F28X50LP between 2001 April 27 and 1998 November 14. A new feature slightly eastward of HS 10-040 is apparent once HS 1-029 is removed, and faint signatures from P.A.s

<sup>&</sup>lt;sup>6</sup>At the systemic recessional velocity of SN 1987A ( $-289 \text{ km s}^{-1}$ ), the F656N filter transmits in vacuo more efficiently [N II]  $\lambda$ 6548 than H $\alpha$ , using pre-launch filter curves. Since no concurrent images in F656N and F658N have been taken, it is not straightforward to measure a monochromatic flux in H $\alpha$  through this filter.

 $163^{\circ}$ ,  $248^{\circ}$  and  $314^{\circ}$  also appear.

To create a systematic observing strategy which maximizes the information gathered in a single spectrum, while dovetailing with previous observations with STIS, we imaged the entire ER in the G750M grating with the same 2" slit orientation as the 1997 April spectrum for the 2000 May and 2001 April observations, and rotated by  $180^{\circ}$  for 2000 October. This produces spatially-resolved monochromatic images of the entire ER in a large number of transitions with a velocity scale of  $\sim 25 \text{ km s}^{-1} \text{ pix}^{-1}$ . Since the ER has a rest-frame expansion velocity of  $10.3 \text{ km s}^{-1}$  (Crotts & Heathcote 1991), even nascent hot spots are clearly detectable by the Doppler shifting of their high-velocity emission away from the ER. Furthermore, the identical slit orientations allow direct spectral image subtraction from previous epochs, preserving data quality while easily removing the background ER flux. Results reported from Paper I were generated from a direct subtraction of the 1997 and 2000 May spectra, however since the 2000 October spectrum has no identically-oriented antecedent, we scaled the neighboring [N II]  $\lambda 6583$  image to remove the H $\alpha$  ER image. The flux of HS 1-029 was 15 times greater in H $\alpha$  than [N II] in a 0".1 STIS spectrum from 1999 August 30, hence this ER removal should not affect the discovery of new spots. In Figure 3d, we see an asymmetric tail toward the east from HS 1-029, identified by Sugerman, Lawrence & Crotts (2000) as HS 10-040, as well as a faint smear at the location of HS 11-355. Furthermore, marginal detections are seen at approximate P.A.s 170°, 250°, and 315°. Figures 3e-f show direct spectral subtractions of the 2001 April H $\alpha$  image from that taken in 1997 April and 2000 May, respectively. Since the slit is oppositely oriented from that in panel (d), the direction of Doppler shifting is reversed. HS 11-355 is unambiguous, as are spectral smears around P.A. 50° and 250°; a faint signature is detected at P.A. 165° and we again note the marginal flux around P.A. 315°. Sugerman, Lawrence & Crotts (2001a) identified these bright new features as HS 12-050, HS 13-165 and HS 14-249, while the flux at P.A. 315°, although very suggestive, is still too faint to reliably distinguish it from noise.

Comparison of the roughly concurrent STIS and ground-based He I images from early 2001 reveals at least some subset of the population of young spots distributed about the ER which we inferred from the He I data. Interpretation of the more recent ground-based imaging from 2001 November is ambiguous, given the high-resolution STIS antecedent. It is possible, and not without precedent, that additional hot spots have appeared, resulting in the nearly-complete brightening about the ER seen in Figure 2h. The spots reported above have certainly brightened as well, and at the ground-based resolution, spots separated by 20–30° will appear unresolved. A spot's light curve can accelerate quite dramatically in short periods of time, as we show in §3.5, thus it is possible that the extended flux seen around HS 1-029 in Figure 2h is due to sudden brightening of spots 10–12. Questions such as these can only be resolved from *HST* imaging, and given the rapid variation manifest in

the number and fluxes of hot spots, systematically-planned observations at *least* twice a year are mandated, if we wish to properly monitor the sequence of spot appearance and their evolution.

## 3.2. Hot Spot Locations

Using both the WFPC2 and STIS imaging data affords us a large set in which we measure the positions of all currently detected hot spots. We measure the flux center of the SN in the WFPC2 data using the F675W image from 1994. The wide passband ensures that higher-velocity emission in the bright optical lines of H $\alpha$  and [N II] will be included, while at this early date the optical ejecta was resolved but still relatively compact and appeared symmetric. We then geometrically registered this image to the STIS data, and used the centroid in this frame for STIS measurements. Centroids for individual hot spots were measured using the PSF-fitting routines within daophot applied to each difference image in which the spot is unambiguously detected. Using the positional uncertainties presented in §4, we calculate the weighted average and weighted variance of the measured centroids of each spot in each difference-image pair. The resulting positions, relative to the measured SN centroid, are presented in Table 1. Quoted errors are the probable uncertainties in each parameter, given by the weighted variance of each set of spot positions, but do not take into account any systematic uncertainty in our adopted SN centroid. We will address this in a forthcoming paper on astrometry of the SN and surrounding field stars. Preliminary results indicate that our measured centroid is consistent with accurate astrometry of the SN in 1987 (Reynolds et al. 1995) using VLBI and *Hipparcos* positional data.

The orientation of the ER and locations of hot spots are shown in Figure 4. Spots are marked by cross-hairs, and confirmed spots are labeled by their IDs. As noted by Sugerman, Lawrence & Crotts (2000), the continued lack of brightening, and inward radial positions of spots HS 8-064 and HS 9-075 appear more consistent with reverse-shock emission than as ejecta-ER interaction (Paper I). We mark their locations by " $\times$ " for clarity, but hereafter remove them from the hot spot list. Spot positions are also indicated around the ER in Figures 7a and 7c. As suggested by both HST and ground-based He I imaging, this system has undergone a notable transition within the last year, from a few distinct hot spots at isolated locations to a nearly continuous distribution around the ER, with few breaks larger than  $45^{\circ}$  in P.A.

An obvious exercise to perform with this positional data is to search for motion of hot spot centroids in time. At the time of writing this paper, only the first three hot spots have been sufficiently bright for enough of an extended period of time to test for proper motion.

We plot in Figure 5 the radial distance of these spots from the SN as measured in filters containing  $H\alpha$ , for those epochs in which each spot has an unambiguous profile for centering. The top half of each panel shows the observed (or "projected," assuming the ER is a circular ring inclined to the line of sight) radial position of each spot versus observation date. The bottom panel shows the deprojected distance of the spot from the SN, using the geometric parameters determined in §3.3. For each locus of points, we show the best-fit line through the data, determined by standard linear least-squares. The slopes of these lines give the proper motion of the centroid of each hot spot, and are listed in Table 2. We denote the velocity of the centroid by  $v_{spot}$ , which for the three spots listed have an average value of  $2000-3000 \text{ km s}^{-1}$ .

Field stars within the LMC should not have significant proper motion over the time period considered, thus the measured positions of these stars serve as estimates of our expected random uncertainty. We plot the radial distance of three stars (of different flux) from the SN in Figure 6. Values along the y-axis have been offset by scalars such that the brightest star is at the top of the figure. Since the band-pass of the F28X50LP filter is wider than that of F675W, which in turn is wider than F656N, a bright star in the former appears faint in the latter. As such, the faintest of the three stars was not detectable in F656N. We list in Table 2 the slope of the best-fit line through each star's position, and find these are consistent with no proper motion, as expected. The flux of Field Star 1 is similar to that of HS 1-029 in F656N, but is far brighter than any spot in F675W or F28X50LP; Field Star 2 is representative of HS 1-029 in the wide-pass filters, and a faint spot in F656N; and Field Star 3 is similar to a faint spot in the wide-band filters. Using the above guidelines, HS 1-029 is "bright" and and HS 2-104 and HS 3-126 are "faint" in most of the epochs considered. We see that the probable errors in the best-fit slopes of the projected data are fairly consistent with a random noise model; the deprojected errors are larger in part due to uncertainties in the geometric parameters of the ER.

#### 3.3. Geometric Parameters of the ER

To accurately interpret the positions of the hot spots on the ER, we begin by studying the ER geometry. A more detailed description of the procedures will be presented in a forthcoming paper. Briefly, we generated an image of the ER at 0″.02278 pix<sup>-1</sup> resolution (double the PC-chip) by drizzling (Fruchter & Hook 1998) data at 2:1 resampling from the F656N and F658N filters (H $\alpha$ +[N II]) between 1994 and 1996. HS 1-029 emission was low, but non-negligible in 1996, and we removed its contributions to the ER by subtracting Tiny Tim model PSFs scaled to the HS 1-029 fluxes as determined in §3.5.

The SN ejecta and outer ring contributions were masked out, then Levenburg-Marquardt least-squares minimization (Press et al. 1992) was used to find the best-fit ellipse to isophotes of the ER flux. Since the flux distribution in the ER is not uniform, but is generally brighter to the northwest quadrant (Sugerman, Lawrence, & Crotts 2001b; Plait et al. 1995), it is important that the flux be normalized in a manner which does not give excess geometric weight to any part of the ring, while still allowing the ER to be distinguished from "the shelf" to the northeast (Plait et al. 1995) and low-level surrounding flux. We achieved this by splitting the ER into N wedges of equal angular size, and normalizing the pixels in each wedge by the second-largest pixel value in that wedge. This choice of normalization factor was made to avoid contamination by bad pixels or low-probability Gaussian outliers. Isophotes of the ER were constructed by including only the upper fraction f of the normalized flux from each wedge, where each wedge flux was integrated in order of descending pixel value. We fit a general ellipse with the center  $(x_0, y_0)$ , axes (a, b) and rotation angle  $\phi$  as free parameters to the ER, using isophotes for  $0.95 \le f \le 0.5$  in steps of 0.01, then averaged the resulting parameters together for a variety of values of N. These choices of f correspond to the elliptical annuli containing 80% and 20% (respectively) of the total ER flux within 1".6. Assuming the ER is a circular ring, inclined to the line of sight by i, then  $i = \cos^{-1} b/a$ . The P.A. of the major axis is the rotation angle  $\phi$ . The resulting values are listed in Table 3, where reported errors are variances only. We will test the presence of systematics within our method in a (aforementioned) forthcoming paper; an estimate of  $\frac{1}{2}$  pixel, or  $\pm 0$ .011 is suggested as a combined uncertainty in axis lengths and SN centroid.

We compare our data with those from Plait et al. (1995) and Burrows et al. (1995) in Table 3. Plait et al. (1995) performed a careful study of the ER geometry using Pre-COSTAR WFPC and FOC images of SN 1987A, predominantly in [O III], but also including [N II] at lower signal-to-noise. Burrows et al. (1995) performed a similar study using WFPC2 images in F502N, F547M, and F656N. Our results are generally consistent with previous values. Of note, we find that the ER centroid is not coincident with our measured value for that of the SN, as also found by Plait et al. (1995). The high-resolution  $H\alpha+[N\ II]$  image is shown in Figure 7a, with the ellipse characterized by our best-fit parameters drawn as a white dashed line. The major and minor axes have been drawn in black, showing the rotated P.A. of the major axis as well as the offset centroid from that of the SN. Tick marks in gray along the minor axis denote light-travel delays of one month. In general the ellipse is a good fit, however a detailed examination reveals considerable scatter about this mean fit. This is more easily seen when the ER has been deprojected and unrolled into a map of observed P.A. versus rest-frame distance from the SN centroid, shown in Figure 7b. For clarity, a fainter stretch of the same data has been plotted in Figure 7c, with contours to highlight structure. The dotted curve is the deprojected best-fit ellipse, and takes on the sinusoidal

shape since the SN and ER centroids do not coincide. A pure circular ring would map to this dotted line, and we see considerable scatter about the mean.

While it is somewhat simplistic to expect the ER, which is clearly seen to be composed of bright knots embedded within tenuous and extended gas, to be a perfect circular ring, it is unclear from this mapping what its true geometry may be. If the ER is inherently elliptical [as suggested by Gould (1994); Gould & Uza (1998)], we would expect the P.A.s of extremal recession velocity would not coincide with the measured minor axes, while the nodes would not lie on the major axes; this might be measurable by a detailed, high-resolution (both spatial and in wavelength) spectrum. Rather, if the ER were warped, sections could appear more or less distant from the centroid than the majority of the gas, however this effect could only be distinguished through three-dimensional mapping. Currently, the three-dimensional circumstellar structures mapped in light echoes by Crotts, Kunkel, & Heathcote (1995) have not revealed such a warp in the equatorial plane, however a re-analysis of that data using our improved techniques of PSF-matched difference-imaging (Sugerman et al. 2002) might have the sensitivity to reveal such features, if present.

## 3.4. Deprojected Positions of the Hot Spots

To properly study the hot spot positions, they have been deprojected using the ER geometry from Table 3, assuming the ER is intrinsically circular and that the SN is at a distance of 50 kpc. Results are listed in Table 1 and have been plotted with their associated statistical uncertainties in Figure 7c. Also listed in Table 1 are  $t_{earliest}$ , the earliest epoch at which the spot is unambiguously detected in HST images;  $\Delta t_{light}$ , the number of days of light-delay between the spot and the SN centroids; and  $v_{blast}$ , the blast velocity required to travel from the radial distance of 0'.6 at day 1300 to a spot given its position and earliest detection, and including corrections for light-travel delays. This is the rough position and epoch at which radio emission first appeared (Manchester et al. 2001). The large uncertainties in  $v_{blast}$  result from large distance to the SN combined with the small angular size of the ER. We caution that this parameter greatly oversimplifies the system: we assume a spherically-symmetric blast-wave expansion at early times, that hot spots are all located within the plane of the ER, we use a somewhat uncertain radial distance from super-resolved radio data, and we ignore the variable cooling time ( $t_c$ , see §5.1) necessary for newly-shocked gas to cool into the optically-emitting regime. Velocities increase by

$$\Delta v_{blast} = \frac{8.68 \times 10^7 d_{50} (r_d - 0'.6) t_c}{(t_{earliest} + \Delta t_{light} - 1300^{d} - t_c)^2} \text{ km s}^{-1}$$
(1)

where  $r_d$  is the spot's deprojected position in arcseconds,  $d_{50}$  is the distance to the SN in units of 50 kpc, and times are given in days. Quoted uncertainties in  $v_{blast}$  to not attempt to account for this unknown parameter, however we list in the final column of Table 1  $\Delta v_{blast}$ , the velocity by which  $v_{blast}$  would increase if  $t_c = 1$  yr is included. While  $v_{blast}$  is not intended for quantitatively predictive purposes, it is instructive when considering the required asymmetry of the system.

## 3.5. Evolution of the Hot Spots

Although first reported in STIS spectroscopy from 1997 April, HS 1-029 is clearly detectable in 1996 in F502N, F555W, F675W, and F658N, and is seen faintly in F555W and F675W in 1995 imaging (as noted by Michael 2000, and clearly demonstrated in Paper I). A long time series of data exists in multiple WFPC2 wave bands for HS 1-029, while a very well-sampled series of images are available for all spots in the very broad STIS F28X50LP images. We study the hot spot evolution by generating multi-wavelength light curves for all spots, plotted in Figures 8 and 9. All photometry was performed using the PSF-fitting algorithm allstar in daophot (see §4). All error bars represent formally-propagated photon-count noise, sky uncertainty and photometry error from PSF-fitting, but ignore unknown systematics such as photometric calibrations.

We present in Figure 8 light curves for HS 1-029 in WFPC2 filters. Data points have been measured from images differenced from the earliest epoch in each filter. Panel (d) displays the combined data from the F656N and F658N filters, both of which contain the dominant  $H\alpha$  hot spot emission. The data points from 1999 April (day 4440) in panels (b), (d) and (e) show an apparent "glitch" in the light curve of HS 1-029, to which we return shortly. Light curves in all filters have roughly similar evolution in spite of the different emission lines contributing to each wavelength range. Using an implementation of the Levenberg-Marquardt non-linear least-squares minimization (Press et al. 1992), we fit simple analytic functions to these curves in an attempt to quantify this first hot spot's evolution. A power law of the form  $A(t-t_0)^b$  describes the data well, however a wide range of parameters offer equally satisfactory fits, since e.g., variation of A compensates for decreasing  $t_0$  and increasing index b. We find  $b \sim 5.5$  yields reasonable fits for all filters, but requires  $t_0 \sim 500-2000$  days. If  $t_0$  represents the initial turn on of the hot spot, these small values are unphysical. If we set  $t_0 = 2500$ , corresponding to the earliest WFPC2 observation, we find  $b \sim 3-3.5$ . A simple exponential  $Ae^{bt}$  fits all the data well with  $b \sim (1.3-1.7) \times 10^{-3} \text{day}^{-1}$ , as does a standard Gaussian  $Ae^{-(t-t_0)^2/\sigma^2}$ , with parameters  $t_0 \sim 5400-5600$  days and  $\sigma \sim 1000-1300$  days.

In Figure 9a–n, we plot the light curves through filters containing  $H\alpha$ , for all confirmed

spots except HS 6-229. An accurate flux for this spot is difficult to measure since it is roughly coincident with star 5; difference images scaled to the ring flux leave residuals of Star 5, and photometrically-scaled difference images do not compensate for the fading ring flux. Since HS 1-029 turned on before the earliest F28X50LP observation by STIS in 1997 December, we measure the 1997 flux in this spot by differencing the earliest STIS image from the 1994 September PC image in F675W, after having been been geometrically registered to the STIS plate scale. All HS 1-029 fluxes from F28X50LP have had this flux from 1997 added back in. All other data points represent averages of the fluxes measured from images differenced from multiple epochs before a given spot turned on. To overplot fluxes from three different filters, we determined an empirical scaling between F28X50LP flux (in counts  $\sec^{-1}$ ) and calibrated WFPC2 fluxes (in ergs  $\csc^{-2}$  s<sup>-1</sup>) using HS 1-029 measured in 2000 February by both imagers. For clarity, a representational  $1\sigma$  error bar is only plotted on the last data point in each panel.

Examination of panel (a) indicates that a short pause did occur after 1999 February, during which the hot spot flux remained depressed from an extrapolated brightening profile until early 1999 October. To ensure that this is not due to calibration errors, we found field stars with fluxes similar to that of HS 1-029 and which are constant to within 2.5%, as measured in data exclusive of 1999 August—October. Photometry for five of these stars for individual cosmic-ray split pairs of images between 1999 August—October is shown in Figure 10a. If the glitch resulted from calibration errors in the data, these light curves would reflect the same trend. That the curves are constant indicates that any variation in the data from this period is real. To test for short-term "flickering" in HS 1-029, we plot in Figure 10b the light curve for the hot spot, generated from the same individual observations as panel (a), differenced from the 1997 December STIS image. We see little evidence for short-term variations aside from a marginally-significant change during the 27 hours separating the first 3 data points, which we trace to bad-pixel contamination of the hot spot in one image.

The light curve for HS 1-029 appears to be changing its slope, and perhaps reaching a plateau, in the most recent epochs. This curve is visually suggestive of a Gaussian function, and is best fit with  $t_0 = 5430-5550$  days,  $\sigma = 1100-1200$  days, which should imply a maximum around 2002 January–March, if the brightening profile is Gaussian. These parameters are quite consistent with those derived from the WFPC2-only light curves, which did not contain the last three data points showing the break in slope. We re-address this in §5.1.

Other hot spots appear to evolve along one of two rough classifications. HS 3-126 and HS 4-091 brighten almost linearly in time from the earliest detection, while HS 2-104 and HS 5-139 accelerate markedly after a period of slow growth, describing a somewhat more exponential evolution. If HS 1-029 is an indication of general hot spot evolution, each light

curve could plateau after an as-yet-unknown period of growth. The evolution of HS 7-289 is somewhat unclear since its most recent datum is depressed relative to either linear or exponential growth, suggesting a possible break similar to, but much more rapid than, HS 1-029. Although much younger than the first four spots, HS 11-355, HS 12-050, and HS 14-249 currently appear to follow the exponential growth pattern while HS 10-040 could be increasing linearly; HS 13-165 (and realistically, most of these newer spots) is too faint for a reasonable assessment as of 2001 April.

## 3.6. Aggregate Evolution of the ER-Ejecta Interaction

The sum of the light curves in Figure 9a–n gives the aggregate flux of the ER-ejecta interaction. We plot this total spot flux in each filter in Figure 9o; this would be the observed light curve (corrected for the fading underlying ER material) if the SNR were fully unresolved in our imaging, i.e. as is typical of ground-based imaging. In Figure 11, we plot total spot flux in He I (measured from data shown in Figure 2). This light curve has an undetermined zero-point, since we have measured the change in He I flux since 1998, at which time HS 1-029 was already a source of line emission. Since these data have not yet been photometrically calibrated, we present them in units of instrumental counts per second.

Suzuki, Shigeyama & Nomoto (1993), Masai & Nomoto (1994), and Borkowski, Blondin & McCray (1997b) have modeled X-ray light curves for the ER-ejecta interaction, but did not address soft UV or optical transitions. Luo & McCray (1991) modeled the impact in the soft UV, but only Luo, McCray & Slavin (1994) directly addressed the expected optical emission, by assuming isotropic ejecta impact an idealized toroidal ring. Using the empirical scaling between F28X50LP and F656N, the total flux in all spots has grown monotonically to  $5 \times 10^{-14} \text{ ergs cm}^{-2} \text{ s}^{-1}$  in roughly six years. Since the hot spot emission is dominated by  $H\alpha$ , we compare this value to the Luo, McCray & Slavin (1994) models, which reach the same line flux far more rapidly: 0.25, 0.75, 0.7, and 0.65 years after the line emission begins (for density models A, B, C, and D respectively). Following a nearly instantaneous turn-on, models A, B, and D grow roughly linearly to a peak and turn over in approximately 1.5, 3.5 and 3 years, respectively, while model C is still brightening (in bursts) after 6.5 years. In contrast, the observed evolution at the time of publication is quite gradual and has yet to plateau. Finally, the predicted model flux for the latest data reported in this paper should be between  $10^{-13}$ – $10^{-12}$  ergs cm<sup>-2</sup> s<sup>-1</sup>, having already passed the maximum peak flux. It is not surprising that this model poorly correlates to the observed evolution, since the actual interaction has proven stochastic while their idealized model considered the impact simultaneous along the whole inner surface of a toroidal ER. Furthermore, their model did not consider the blast front propagating through an intervening H II region. It remains to be seen whether the integrated light curve of the ER-ejecta interaction will evolve like one of these models once the ejecta impact the main inward surface of the ring.

## 4. Consistency and Completeness

As demonstrated by Lawrence & Crotts (2000) and noted by Maran et al. (2000), hot spots are most easily detected at early times in spectra, however in the absence of a systematically-planned STIS observing program which samples the entire ER (such as that presented in this work), they are most effectively revealed with PSF-matched difference imaging. As noted in §2, hot pixels constitute a significant source of contamination and confusion in HST data, and the accurate detection of new hot spots at early times depends entirely on our ability to distinguish them from the abundant sources of noise. Proper detection of this rapidly-changing phenomenon requires confirmation in multiple epochs of data, however high-resolution data are relatively sparse: WFPC2 imaging is taken roughly only once per year, and STIS spectra are predominantly narrow-slit slices through the ER rather than 2" spectral images of the entire ring. While we make every effort to maximize the data quality of HST imaging to reliably detect new loci of interaction along the ER, it is important to understand the limitations inherent to these data.

To test the reliability of new hot spot detection, we generated artificial data as follows. All known hot spots were removed from the F656N images from 1999 January and 1999 April using a Tiny Tim model PSF, then 10 pairs of images were created, each containing a random number of hot spots (average of 5 spots per image), of random flux (ranging from the faintest to brightest actual spot fluxes), situated randomly around the inner-half of the ER (where we observe new spots forming), with the flux of each spot in 1999 April 10% brighter than 1999 January. These data were differenced from F656N images from 1998 and 1997, and analyzed using the same criteria as applied to actual spot detection. Table 4 contains the results from this exercise. For each given flux range,  $N_{\text{Detected}}$  is the total number of sources we identified in all images,  $N_{\text{False}}$  is the number of sources which were not actual spots, and  $N_{\text{Missed}}$  is the number of actual spots which we missed. We see that our detection procedure is  $\sim 100\%$  complete for the majority of the applicable flux range, and roughly 60% complete at the faintest end, corresponding to the very faintest spots (e.g. HS 5-139) at their earliest detections.

The employment of PSF-fitting crowded-field photometric techniques from *daophot* follows from the obvious crowding in some hot spot regions, but also from the noise characteristics of the data. As seen in Figure 3, hot spots lie on the inner edge of the ER, translating

in difference images to the boundary between the uniform region interior to the ring, and the non-uniformly fading ER. Since the background varies on pixel-to-pixel scales, a large sky annulus will likely not reflect the actual background of the hot spot. Many hot spots are faint, and are more strongly affected by Poisson noise and the omnipresent warm pixel contamination when performing simple aperture photometry. The *allstar* task performs a non-linear least-squares fit of an analytic stellar profile to each source, while dynamically fitting both the underlying sky and nearby sources. This should, in principle, provide the most reliable centroid and flux estimate for a hot spot, by directly addressing the above difficulties.

This was directly tested by generating an additional set of 5 pairs of images with hot spots of random flux placed at the known hot spot positions, differencing them as above, and performing both standard aperture (with *phot*), and crowded-field (with *allstar*) photometry. Photometric accuracy for the latter, and positional accuracy for both algorithms are listed in the final three columns of Table 4. Aperture photometry yielded errors of roughly 50% for fainter sources and in crowded regions. In contrast, *allstar* errors are generally within the formal photometric uncertainties. In most cases, centroids measured with *allstar* are more accurate as well, since flux-weighted centroids often drift toward a brighter nearby source or warm pixel.

#### 5. DISCUSSION

## 5.1. Generalized Hot Spot Evolution

Following the radiative shock model of Michael et al. (2000, and references therein), the SN ejecta expanded at  $\lesssim 3 \times 10^4$  km s<sup>-1</sup> until it encountered an H II region of density  $n_{\rm H\,II}$  interior to the ER, which was formed when the blue supergiant progenitor photoionized stellar winds ejected during its previous red supergiant phase (Chevalier & Dwarkadas 1995). This encounter drove a forward shock into the H II region with a velocity  $v_b$ , which ultimately impacts a protrusion of density n in the ER. The density jump implies the shock propagates into the protrusion with velocity  $v_s = v_b f(\theta) \sqrt{n_{\rm H\,II}/n}$  where  $f(\theta)$  accounts for the obliquity of the shock<sup>7</sup>, and ranges from 2 for a head-on shock to 0.7 for  $\theta = \frac{\pi}{2}$ . The time for the shocked gas to radiatively cool from the postshock  $\sim 10^6$  K to  $\sim 10^4$  K, at which the gas emits largely in the optical, is  $t_c$ . For velocities in the range of a few hundred km s<sup>-1</sup>, Michael

<sup>&</sup>lt;sup>7</sup>These values of  $f(\theta)$  were calculated for a plane-parallel shock impacting a cylinder with density contrast  $n/n_{\rm H\,II} = 70$ , and ignored time-variable effects (E. Michael, private communication).

et al. (2000) report  $t_c = 4.6n_4^{-1} \left(v_s/300 \text{ km s}^{-1}\right)^{3.7} \text{ yr}$ , where  $n_4$  is the density in units of  $10^4$  cm<sup>-3</sup>. With infinite spatial resolution, the optical observation of a new parcel of emitting gas would only show where the shock had been a time  $t_c$  earlier. Since this cooling time is a function of  $v_s$ , n and the chemical composition of the ER, each emitting parcel of gas does so with its own set of these parameters. The hot spots which we observe are the integrated light curves of all the ER material in a seeing element through which the forward shock has passed, and the centroids we measure, derived from regions too small to be resolved by HST, are the luminosity-weighted 2-D projections of 3-D emitting volumes. The observed motion of the hot spot's centroids is thus the measurement of the radial increase in average emitting area in time, and can only serve as a lower limit to the velocity of the shock causing the emission.

Consider what one would observe as the forward blast moves down the side of an inwardfacing protrusion. If one idealizes the protrusion as a cylinder of constant density, the forward shock as planar with constant velocity  $v_b$ , and ignoring optical thickness effects and radiative precursors, then the cooling time  $t_c$  will be constant. As the shock moves down the cylinder, the transmitted shock velocity  $v_s$  will be constant and much less than  $v_b$ , thus an observation at infinite resolution would show a uniform growth of emission down the axis at velocity  $v_b$ . At our limited resolution, we instead observe the flux-barycenter of all emitting material, and hence measure a velocity equal to  $\frac{1}{2}v_b$ . For a similarly constructed conical (or truncated cone) protrusion, the observed velocity would be  $\frac{2}{3}v_b$ . Of course, an actual protrusion has a complicated (and as yet unknown) geometry and density structure, both of which mediate the variation of the cooling timescale and the mass (per unit time) swept-up by the forward blast, as the blast moves down the protrusion. Nonetheless, from geometry alone we expect the observed spot velocity to be of order half the blast velocity. From Table 1,  $v_{blast}$  is the inferred blast velocity needed to reach a given spot, assuming the blast expanded uniformly to 0".6 during the first  $\sim 1300$  days, and has an average value of  $\sim 3000-5000$  km s<sup>-1</sup> for most spots. Recall that these values do not include estimates for  $t_c$ , which would increase these inferred velocities by hundreds of km  $\rm s^{-1}$  per year of cooling time (Eq. 1). Assuming a 1–2 yr cooling time, we find the values of  $v_{blast}$  are of order 1–2 times those of  $v_{spot}$ , consistent with the heuristic expectation above. We thus interpret  $v_{spot}$  as a rough measurement of half the blast velocity, implying  $v_b \sim 3000 - 5000 \text{ km s}^{-1}$ .

Hot spot evolution is now considered according to the following scenario. A hot spot arises on an inward-facing protrusion from the ER, as shown in Figure 3 of Michael et al. (2000). From the radiative shock model,  $t_c \propto f(\theta)^{3.7}$  thus the time at which post-shocked gas actually emits visible line radiation is a sensitive function of the obliquity of the shock. The blast wave first strikes the tip of the protrusion head-on, and thus has a long cooling time (since  $f(0) \sim 2$ ). As the blast wave travels down the length of the protrusion,  $f(\theta) \to 0.7$ 

hence  $t_c$  decreases substantially. For  $v_b = 3000 \text{ km s}^{-1}$  and  $n = 10^4 \text{ cm}^{-3}$ ,  $t_c \sim 60 \text{ yr}$  for a head-on shock, and  $t_c \sim 1$  yr for a side shock. An observed hot spot at early times is thus the shocked gas along the protrusion's sides cooling into an optically-emitting temperature range. Once the shock reaches the base of the protrusion,  $f(\theta) \to 2$  and  $t_c$  increases again. Flux in the early-time light curve will grow substantially as new gas is shocked by the blast wave along the side of the protrusion. Once the blast reaches the protrusion base, emission will be dominated by newly-shocked gas from the slow shocks moving into the protrusion along its sides, and since roughly equal volume will be swept-up per unit time, the light curve should flatten and grow monotonically (assuming the shocked gas does not cool out of the optical for a long time, perhaps due to photoionization from shocked material upstream). Only after many years will the light curve suddenly accelerate again, as the gas at the tip and base cool into the optical-emitting regime. At early times, the tips of the shocked protrusions should be substantial X-ray emitters, while the sides emit optical and near-IR lines. The correlation of a population of X-ray bright spots with optical hot spots (Park et al. 2002) in Chandra imaging is suggestive of this interpretation.

The late-time flattening of the lightcurve of HS 1-029 may be explained via this model. From Figure 7, the protrusion on which HS 1-029 appears is long and fairly isolated from the neighboring ER material. Idealizing this as a truncated conical protrusion of length 0".05-0".1 (as measured in panel b of Figure 7), the forward blast would require roughly 1500–3000 days to travel its length, assuming a velocity of 3000 km s<sup>-1</sup>( $\S 3.2$ ). As shown in  $\S 3.5$ , the light-curve of HS 1-029 shows a significant change in slope beginning sometime around day 4700–5000, i.e. 1800–2200 days after its earliest appearance, and within the expected range noted above. A physical scale of HS 1-029 can be estimated using the radial position of HS 10-040, assuming the forward shock had to pass the HS 1-029 material before impacting that of HS 10-040. The radial position of HS 10-040 is highly uncertain; however, using its central value and the initial radial distance of HS 1-029, the deprojected radial difference in distance is  $\sim 0\rlap.{''}05$ , or  $3.8d_{50}\times 10^{16}$  cm. This is consistent with the value of  $3\times 10^{16}$  cm found by Michael et al. (2000) using spectroscopic considerations, and at this size, the expected time for the break in slope of the light curve of HS 1-029 is consistent with that observed. This is suggestive that the heuristics of our model are correct, and that the forward blast is nearing the inner edge of the ER (rather than a protrusion) in the vicinity of HS 1-029.

Our model also suggests a possible explanation for the linear light curves of spots 2–5. If these protrusions are small in radial extent, the time necessary for the shock to move down their sides is greatly reduced, hence the spot's emission would spend little time in the initial rapid-brightening phase, and would quickly display the more monotonic increase in flux consistent with the transmitted shock moving into its sides. If this interpretation is correct, the observed light-curves of the first five spots thus suggest that HS 1-029 lies on a

longer radial protrusion than that of HS 2-104 or HS 5-139, which in turn are longer than HS 3-126 or HS 4-091.

# 5.2. Hot Spot Timing

Why did HS 1-029 turn on over three years prior to any others? Is there something unique about this spot which requires a separate physical explanation? Figure 4 suggests that hot spots occur on inward-facing protrusions from the main ER, which would naturally be the first sites to be struck by an isotropically-expanding forward blast wave. From Figure 7, we see that nearly all spots do appear to lie at the extrema of inward-facing protrusions. Furthermore, HS 1-029 is located, in the deprojected frame, on the most inward-facing protrusion, and from Figure 5 we see that its early-time position was roughly 0''.06 closer to the SN than other spots. Examination of the values of  $v_{blast}$  in Table 1, which were calculated using the early-time positions of spots, suggests that there was no preferential velocity required for HS 1-029 to turn on as early as it did. Rather, we argue that the early appearance of HS 1-029 results mainly from its inward position with respect to the other hot spot protrusions.

Values of  $v_{blast}$  for all spots are suggestive of a roughly uniform blast velocity of 3000– 5000 km s<sup>-1</sup>, consistent with that inferred in the radio by Manchester et al. (2001), in HST spectroscopy by Michael et al. (2000), in Chandra X-ray imaging ( $v \sim 5200 \pm 2100$ km s<sup>-1</sup>) by Park et al. (2002) and in Chandra X-ray spectra ( $v \sim 3400 \pm 700 \text{ km s}^{-1}$ ) by Michael et al. (2001). We now explore whether we can glean additional information about the forward blast from the observed positions and earliest appearance of the hot spots. If we use  $t_{earliest} + \Delta t_{light}$  as a relative estimate (with respect to the SN) of when a hot spot first turned on, the following spots are mutually coeval: spots 2 and 3; spots 4 through 6; spots 10 and 13; and spots 11, 12, and 14. Since HS 2-104 and HS 3-126 have nearly identical deprojected distances and values of  $v_{blast}$ , there is no need to invoke significant inhomogeneity in the forward blast to explain the order of the appearance of these neighboring spots. Spots 4-6, however, suggest a different trend. The deprojected distances of HS 4-091 and HS 6-229 are marginally discrepant at the  $1\sigma$  level, implying that the blast wave had to travel significantly faster to HS 6-229 for it to turn on at the same time as HS 4-091. Although the uncertainties are large, hot spot positions suggest a rough trend that the required shock velocity varies somewhat continuously with P.A., lowest to the north and northeast around HS 11-355 and HS 1-029, and increasing to the west around HS 6-229 and HS 7-289. This could also be explained by invoking variations in shapes of the protrusions hosting the hot spots, since the cooling time  $t_c$  is such a strong function of geometry.

Inspection of the locations of spots around the ER shows that roughly  $\frac{3}{4}$  of confirmed spots are located along the eastern half of the ring. This would be the natural result were the forward blast to arrive at that half first. This suggests two possible explanations. First, the SN centroid is offset to the east of that of the ER. Recall that in §3.3, we find our measured SN centroid is offset by 20 mas to the east of the ER centroid. We also find in Table 1 that eastern spots appear closer (in the deprojected frame) to the SN than those in the west. A simple assumption of symmetry suggests that the deprojected positions of hot spots should be roughly equidistant from the SN, implying that our measured SN centroid might be inaccurate, perhaps due to asymmetry in the ejecta in 1994, or patchy absorption from dust within the ejecta (as suggested by our referee). We quickly tested this by measuring spot positions from the ER centroid, and found that while this does result in an increase of the deprojected distance of easterly spots and a decrease for westerly spots, the overall effect is not large enough to fully reconcile the discrepant distances presented. Recalling that spots appear on inward-facing protrusions, we may speculate that in addition to an offset SN centroid, spots to the east may lie on systematically-longer protrusions. With the data currently presented, we can not rule out this hypothesis or the first explanation.

Second, an inhomogeneity in the forward-blast exists on the largest scale. Michael (2000) find from narrow-slit STIS spectra that the reverse shock is roughly 5% further from the SN at P.A.~220° than at P.A.~40°, concluding that CSM interior to the ER is more tenuous along the far (southwestern) side of the ring. Recent images of the radio (Manchester et al. 2001) and X-ray (Burrows et al. 2000) remnants both show increased emission toward the eastern side of the ER. Burrows et al. (2000) interprets the bulk of the X-ray and non-thermal radio emission as arising from a zone of shocked SN debris and CSM between the forward blast and reverse shock. A detailed study of Chandra X-ray imaging (Park et al. 2002) shows that X-ray bright knots are well correlated with the optical hot spots, however Michael et al. (2001) argue that only  $\sim 4\%$  of the X-ray emission can come from these spots, and suggest that the observed X-ray asymmetry is indicative of denser CSM material to the east interacting with the blast wave. This, they propose, could result from either an asymmetric SN explosion or an asymmetric CSM, as follows. If the SN explosion is symmetric, and the CSM is denser to the east, then the forward blast would travel faster into the western half of the ER. Conversely, if the CSM is symmetric, then the blast wave must have travelled faster in the eastern direction, shocking denser CSM closer to the ER.

We briefly consider this latter scenario. If the increased radio emission to the east results uniquely from a higher blast velocity toward that half of the ring, we should expect the western emission to mimic that in the east with a roughly constant time delay. Comparison of super-resolved images of SNR 1987A from Manchester et al. (2001) show that the western radio emission in 1999.7 and 2000.8 is at roughly the same flux as eastern emission in 1995.7

and 1996.7, respectively. Continued monitoring of the radio remnant will show whether this four-year time-delay is persistent.

Consider now the former scenario, in which the CSM is asymmetric. The three-ring nebulosity surrounding the SN has largely been attributed to the interaction of the progenitor star's blue and red supergiant (BSG and RSG) winds via the interacting stellar winds model (Kwok 1982; Balick, Preston & Icke 1987). Equatorial overdensities in a previously-expelled slow, dense wind focus a fast, tenuous wind into a polar trajectory, the interaction from which produces a bipolar peanut-shaped nebula, or wind-blown bubble (Woosley 1988; Arnett et al. 1989; Chevalier & Emmering 1989; Luo & McCray 1991; Wang & Mazzali 1992). The ER is the overdense waist of the peanut, the inside of which was largely evacuated by the BSG wind. The visible ring is most likely the inner skin of the overdensity, which was optically thick to the UV and soft X-ray flash from the SN, but is optically thin to the cooling line emission we now observe. If the RSG circumstellar outflow had been denser toward the eastern half of the equatorial plane, then the inner cavity which the BSG wind carved out would have been closer to the central star in that direction than toward the west. This would have resulted in an observed ER that is offset from the SN centroid, and an overall density enhancement within the equatorial plane to the east. While we can not rule out an asymmetric explosion, values of  $v_{blast}$  suggest the shock is traveling faster into the western half of the ER, i.e. that the asymmetry lies in the CSM. We thus favor the equatorial density enhancement proposed above, which may explain both the offset ER centroid and proposed CSM asymmetry. This situation should have left its imprint on the geometry of the contact discontinuity between the RSG wind and the previously-equilibrated bubble filled by the progenitor's main sequence wind (Chevalier & Emmering 1989). This interface was found by Crotts, Kunkel, & Heathcote (1995) at 9"-15" in light echoes, and will be tested in a re-examination of those data by Sugerman et al. (2002).

While the above work suggests that a fairly isotropic blast wave can explain the appearance of most spots, it is unlikely that the blast wave has traveled uniformly (or continues to) in all directions into a visibly inhomogeneous medium. As the forward shock approaches the ER, it must encounter an increasing density gradient, which will cause it to decelerate on the largest scales. This has been addressed by e.g. Chevalier & Dwarkadas (1995); Borkowski, Blondin & McCray (1997a); and Lundqvist (1999) via the low-density H II region previously mentioned. Chevalier, Blondin & Emmering (1992) find that Rayleigh-Taylor instabilities develop in the contact discontinuity between the shocked H II material and shocked ejecta. These can develop into plumes that redirect previously-reflected shocks back into the ER in spots rather than uniformly (Borkowski, Blondin & McCray 1997b). We therefore expect strong velocity inhomogeneities on small scales. Whether or not this mechanism is responsible for HS 6-229 and HS 7-289 both of which appear further from the SN than neighboring

protrusions (see Figure 7c), is unclear. The probability of a randomly-placed plume impacting an inward-facing protrusion from the ER is low, unless the number density and/or angular size of such plumes is very high. This question is better addressed by hydrodynamic modeling.

We caution the reader of the preliminary nature of these inferences. As noted above, values of  $v_{blast}$  assume an isotropic expansion at early times, and ignore the unknown cooling time  $t_c$ , which roughly dictates when a spot first becomes visible in optical line emission after it has been shocked. From the shock model presented above, we see that  $t_c$  is a strong function of the forward blast velocity, and both the shape and size of the protrusion. At this early stage of hot spot study, all three remain highly uncertain, if not unknown. While our data suggest the forward blast may travel faster in the western direction, HS 14-249, located between HS 6-229 and HS 7-289, does not require an above-average value of  $v_{blast}$  to explain its earliest appearance. Thus, many interpretations of the data exist. The forward blast could be symmetric and fast ( $\sim 5000~{\rm km~s^{-1}}$ ), and HS 6-229 and HS 7-289 lie on protrusions whose geometries yield significantly shorter cooling times (e.g. cylinders) than those of most other spots (e.g. wide cones). In keeping with our proposed scenario, the geometry of HS 14-249 could result in a much longer cooling time than its neighboring two spots, delaying its discovery until after HS 6-229 and HS 7-289. These ambiguous interpretations require a combined observational and computational effort. Continued spectroscopic monitoring of the ER and hot spots will yield better estimates of the physical conditions of the pre- and post-shocked gas, which serve as important constraints for numerical modeling. Radiation-hydrodynamic modeling of the shock interaction with a variety of probable protrusion geometries can offer theoretical light curves and flux proper-motion curves against which data (such as those presented in this paper) can be compared. As such, the conclusions from this work are only preliminary and suggestive, as there is much yet to unfold in this stage of the evolution of SNR 1987A.

Finally, we note that as of 2001 April, there remain protrusions from the ER which do not appear to host hot spots. From Figure 7, we see that hot spots are expected at rough P.A.s of 5°, 85°, 195°, and 310°. While there is a marginal detection of flux at the latter position in 2001 May, no spots have been detected between P.A. 50°–90°, and 170°–220°. The most recent He I data show a smear of flux toward PA 90, suggestive that new spots may be forming in that region, however no significant detection of flux is made between PA 180°–220°. The first appearance of spots in this vicinity should prove another interesting measurement of asymmetry in the forward blast.

# 5.3. ER Ellipticity and Distance to the SN

The analyses of Gould & Uza (1998) suggest that the ER might have an intrinsic ellipticity with axis ratio 0.95, based in part on the discrepancy between the observed ER geometry and that implied by the interpretation of UV line-emission light curves as fluorescent light echoes off the ER (Panagia et al. 1991). Measuring the inclination angle  $i_t$  of the ER from the delay of the UV light echoes, Gould & Uza (1998) find  $i_t = 40^{\circ}.5 \pm 0^{\circ}.5$ . Insertion of our geometric inclination angle  $i_{\theta} = 43^{\circ}.8 \pm 0^{\circ}.13$  into their Equation 4.5 also yields an intrinsic ellipticity  $b/a = \cos i_{\theta}/\cos i_t = 0.95$ . The three-dimensional structure of the hourglass nebula containing the ER (Crotts, Kunkel, & Heathcote 1995) has been reanalyzed by A. P. S. Crotts (as reported in Gould & Uza 1998), revealing again an intrinsic flattening of the ER of  $b/a = 0.95 \pm 0.02$ . The agreement of these two independent measurements is suggestive that the ER may have an intrinsic 5% ellipticity.

An ellipse, when inclined from the line of sight, is mapped to a new ellipse, and can always be rotated about orthogonal axes into a circle (even if that is not its actual shape). We find however that the ER deviates somewhat from even an elliptical morphology. It is unclear at this time what the actual geometry is, however we can envision a number of possibilities. The ring could also be warped, as noted in §3.3, or it could have an inherent radial profile that is not a smooth function of P.A. Recalling the postulated density enhancement to the east, an axially-symmetric outflow would expand furthest into the lowest density medium. Figure 7 shows that the ER material to the northwest is furthest from the SN, suggestive of this simpler interpretation.

Assuming that the ER is planar and circular, Gould & Uza (1998) calculate the distance to the SN as  $D = c(t_+ + t_-)/\theta_+$  where  $t_\pm$  are the times of the two cusps of UV line emission around the ER following the SN explosion, and  $\theta_+$  is the major axis of the ER. Using a re-analysis of IUE data yielding  $t_- = 80.5 \pm 1.7$  days and  $t_+ = 378.3 \pm 4.8$  days, and the geometric data in [O III] from Plait et al. (1995), Gould & Uza find a weighted average distance of  $47.25 \pm 0.76$  kpc. If intrinsic ellipticity of the ER is taken into consideration, Gould & Uza find  $D = c(t_+ + t_-) \cos i_\theta/\theta_-$ , where  $\theta_-$  is the minor axis of the ER, yielding an upper limit distance of  $48.8 \pm 1.1$  kpc. Finally, they consider the case of UV emission arising from the inner edge of the ER, and find  $D < 50.8 \pm 0.9$  kpc. They discount this latter scenario as highly implausible, explaining that N III (seen in the UV echo) has the same ionization potential as O III (used to measure the geometric data), making it unlikely that their physical distribution is dissimilar.

The success of the Gould & Uza method relies on the assumption that  $\theta_{+}$  measures the size of the region from which the UV echo occurred, however the geometric parameters of the ER presented in this work and Plait et al. (1995) only measure the size of the optically-

emitting region at the time the data were taken. Both Plait et al. (1995) and Sugerman, Lawrence, & Crotts (2001b) found in HST imaging that the ER is larger in [O III] than in H $\alpha$  and [N II], and Lundqvist & Sonneborn (1997) find that the [N II]-emitting ER gas has a higher density than that emitting [O III]. Recalling the proposed formation scenario in which the ER lies at the waste of a bipolar "hourglass" nebula of gas, Lundqvist & Sonneborn (1997) offer a simple model in which the [N II]-emitting gas is located within the equatorial plane, while [O III] emission arises from less dense gas along the walls of the hourglass just above or below this plane. The densest gas cools the most rapidly, hence the [N II]-dominated ER seen today should have been dominated by [O III] at earlier times. Given that the [0 III] ER appeared larger than that in [N II] in 1995, it is unlikely that the values of  $\theta_+$  from Plait et al. (1995) or this work measure the position of the dense material which fluoresced to produce the observed UV echo. Rather, this component may have had such a high density that it has faded and is "invisible" in optical line-emission today.

We propose the following pragmatic distance estimate. The best-fit parameters for the ER (§3.3) offer upper limits to the location of the UV-emitting region, while the dense inner edge of the ER, now well delineated by hot spot activity, serves as a reasonable lower limit. Measuring the innermost edge of the ER as the average deprojected position of all hot spots, we find  $\theta_{+,min} = 1.464 \pm 0.054$ , while we take  $\theta_{+,max} = 1.658 \pm 0.026$  from Table 3. Assuming the ER is planar and circular, we now find a lower distance limit of  $47.9 \pm 0.92$ kpc, and an upper limit of  $54.4 \pm 2.1$  kpc. For comparison, Feast (1999) reviews a number of distance determinations to the LMC, finding average values of  $\sim 55$  kpc from Cepheids and around 53.7 kpc from Miras and RR Lyrae, while a few methods do favor a shorter distance of 45–48 kpc, such as that determined via eclipsing binaries. Using red clump stars in HST fields surrounding the SN, Romaniello et al. (2000) determine the distance to the LMC to be  $52.2 \pm 2.3$  kpc. The light echo analyses of Xu, Crotts, & Kunkel (1995) show the SN to be at least  $\frac{1}{2}$  kpc deep into the inclined plane of the LMC, thus the lower distance limit appears inconsistent with these distance indicators. Rather, we find they favor the longer SN distance scale, and thereby suggest that the UV echo did originate along the inner edge of the ER, as traced by the positions of the hot spots.

## 6. Conclusions

We have shown that a hot spot is present, or appears to be developing, on nearly every inward-protrusion or gradient of increasing flux. We expect to see spots developing at rough P.A.s of 5°, 85°, 195°, and 310° in the years 2002-2003, with the currently confirmed spots eventually spreading in P.A. into resolved emission regions. It is *abundantly* clear that hot

spot evolution changes on time scales as short as one month, and dramatically within six months. Observing campaigns, such as the ground-based IR and STIS spectral observations from this work, are mandated to efficiently and completely monitor this rapidly evolving system. To properly interpret current and future observations of this system, models of optical line profiles and intensities, as well as radiative shock models consistent with the observed hot spot loci and evolution, should be further developed.

As Michael et al. (2000) point out, it will not be straightforward to develop a quantitative model of line spectra and evolution of hot spots. It is our hope that the data reported in this work will be combined with that from spectra, yielding detailed information about density and temperature (Lawrence et al. 2002), and shock velocity (Michael et al. 2000), to provide a solid empirical base on which to build appropriate analytic models to both analyze and predict future evolution. Nonetheless, analytic predictions of the ER-ejecta evolution do exist. Of particular interest, Borkowski, Blondin & McCray (1997b) find that the impact should have three periods of brightening, corresponding to the initial impact of the blast wave, the later impact of a reflected shock, and the merging of the two shocks within the ring material. Within this framework, we question whether the "glitch" from HS 1-029 around day 4400 (and perhaps currently occurring in HS 7-289) may correspond to the delay between the first two brightening periods. This should be accompanied by an increase in temperature, density and shock velocity from the hot spot, all measurable through spectroscopy. In the meanwhile, only time will more fully "illuminate" the ER-ejecta evolution.

APSC, SSL and BEKS gratefully acknowledge funding from NASA (NAG5-3502) and STScI (GO-8806 and GO-8872). They are also thankful for the allocation by the director of STScI for discretionary time. BEKS thanks Robert Uglesich for his patient assistance with difference imaging and systems management, Peter Lundqvist and our anonymous referee for their thoughtful comments.

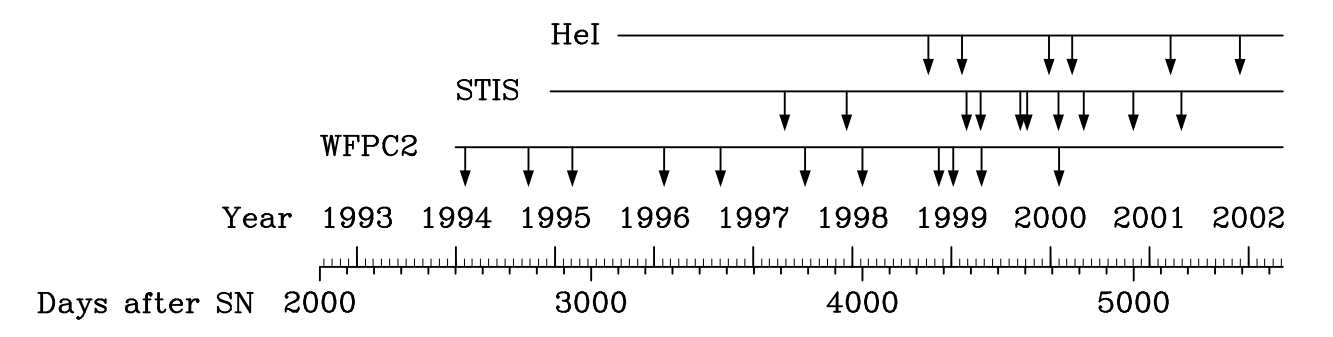


Fig. 1.— Schematic relating calendric dates to the number of days after the SN exploded, as well as showing the dates of the WFPC2, STIS and ground-based He I observations used in this paper.

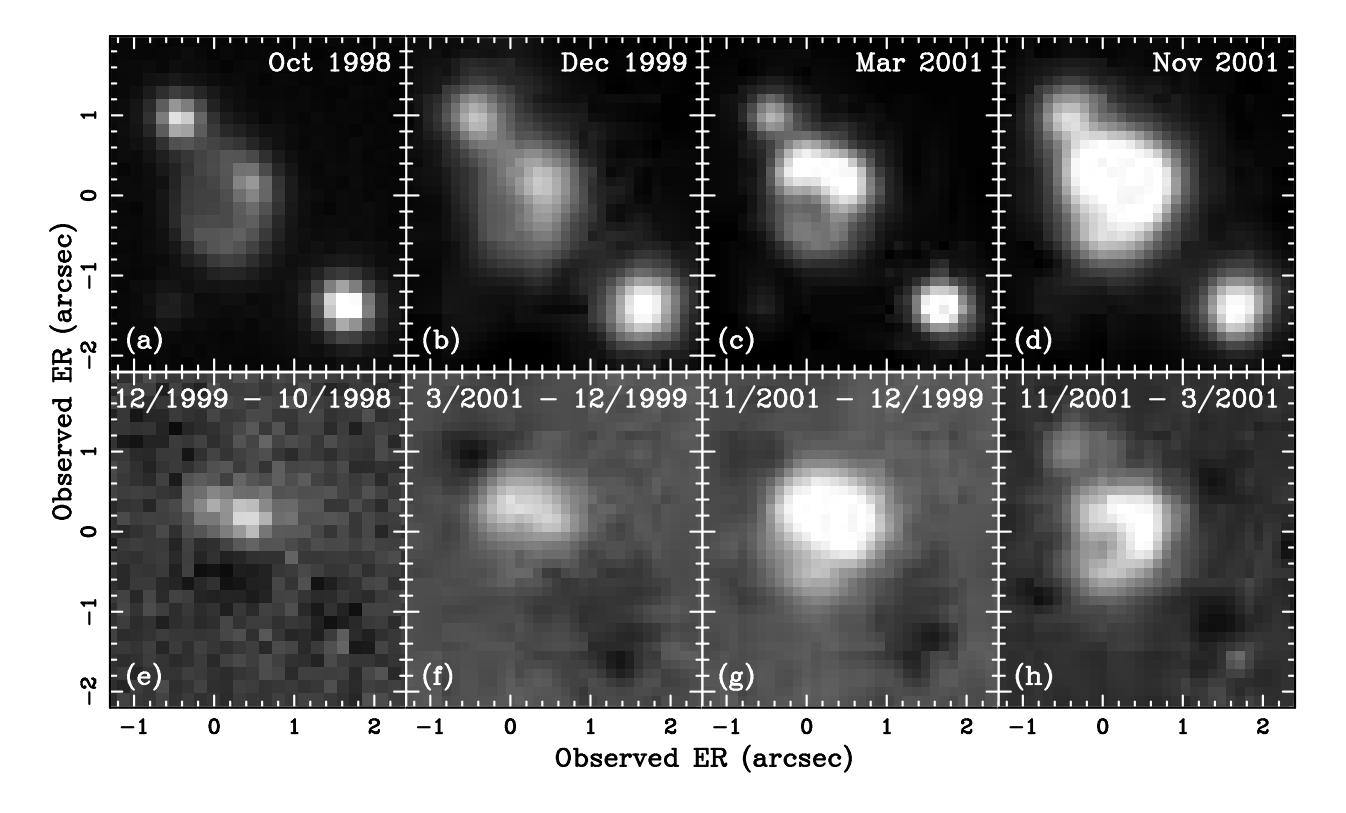


Fig. 2.— Ground based CTIO 4 m He I  $1.083\mu m$  imaging of SNR 1987A. North is to the right and east up. (a) CIRIM data from 1998 October. (b) OSIRIS data from 1999 December. (c) OSIRIS data from 2001 March. (d) OSIRIS data from 2001 November. (e) Difference image between 1999 December and 1998 October. We see the brightening of HS 1-029, the appearance of spots to the southeast, and the fading ER to the west. (f) Difference image between 2001 March and 1999 December. Flux from spots 1–5 continues to increase, and unresolved spots distributed about the ER are now brightening faster than the fading ER material. A small residual of star 2 (lower right) remains since this star's flux is within the non-linear regime of the detector in the 1999 image. (g) Difference image between 2001 November and 1999 December. Flux has dramatically increased along the eastern half of the ER, and the western half is now standing out against the background, suggesting a population of brightening spots. (h) Difference image between 2001 November and 2001 March. This image highlights the smaller-scale changes in flux: spots appear to now be located around the entire ER, except in the south-southwest region. A population of spots surrounding HS 1-029 may explain the "L"-shaped flux distribution in the northeast quadrant. Star 3, at the upper left, is known to be variable, and as seen in the differenceimage sequence, was brighter in 1999 December and 2001 November than in 2001 March.

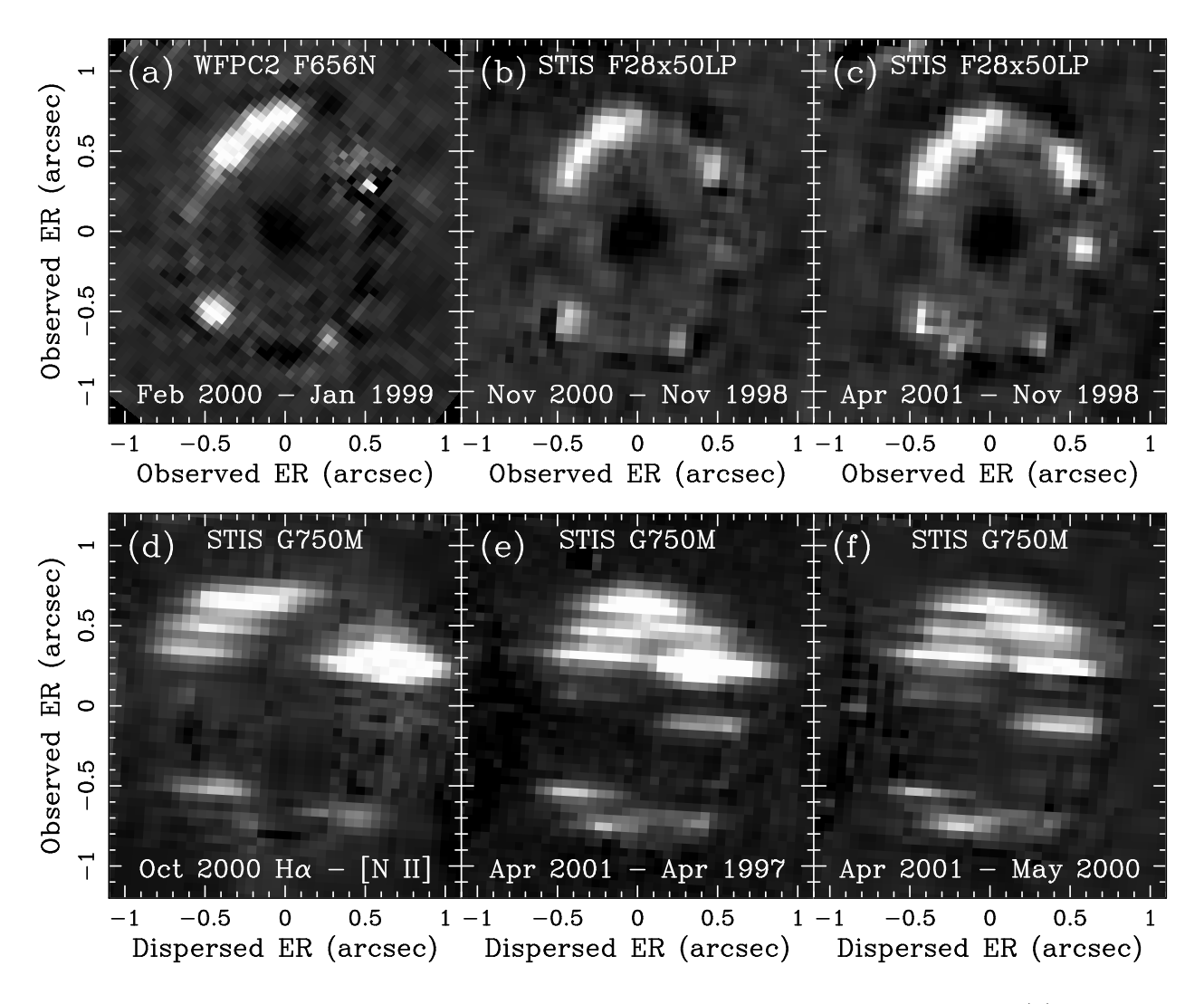


Fig. 3.— HST difference imaging of SNR 1987A. North is right and east is up. (a) WFPC2 F656N difference image between 2000 February and 1999 January. (b) STIS F28X50LP difference image between 2000 November and 1998 November. (c) STIS F28X50LP difference image between 2001 April and 1998 November. HS 1-029 has been removed from images in panels (a)-(c) using a  $Tiny\ Tim$  model PSF. (d) STIS G750M H $\alpha$  spectral image from 2000 October with the [N II]  $\lambda$ 6583 image subtracted away to remove ER flux. In this orientation, wavelength increases to the right. (e)-(f) STIS G750M H $\alpha$  spectral image from 2001 April differenced from identically-oriented H $\alpha$  observations in 1997 April and 2000 May (respectively), to remove ER flux. In this orientation, wavelength increases to the left, and one pixel equals 0.56 Å or  $\sim$  50 km s<sup>-1</sup> of Doppler shift.

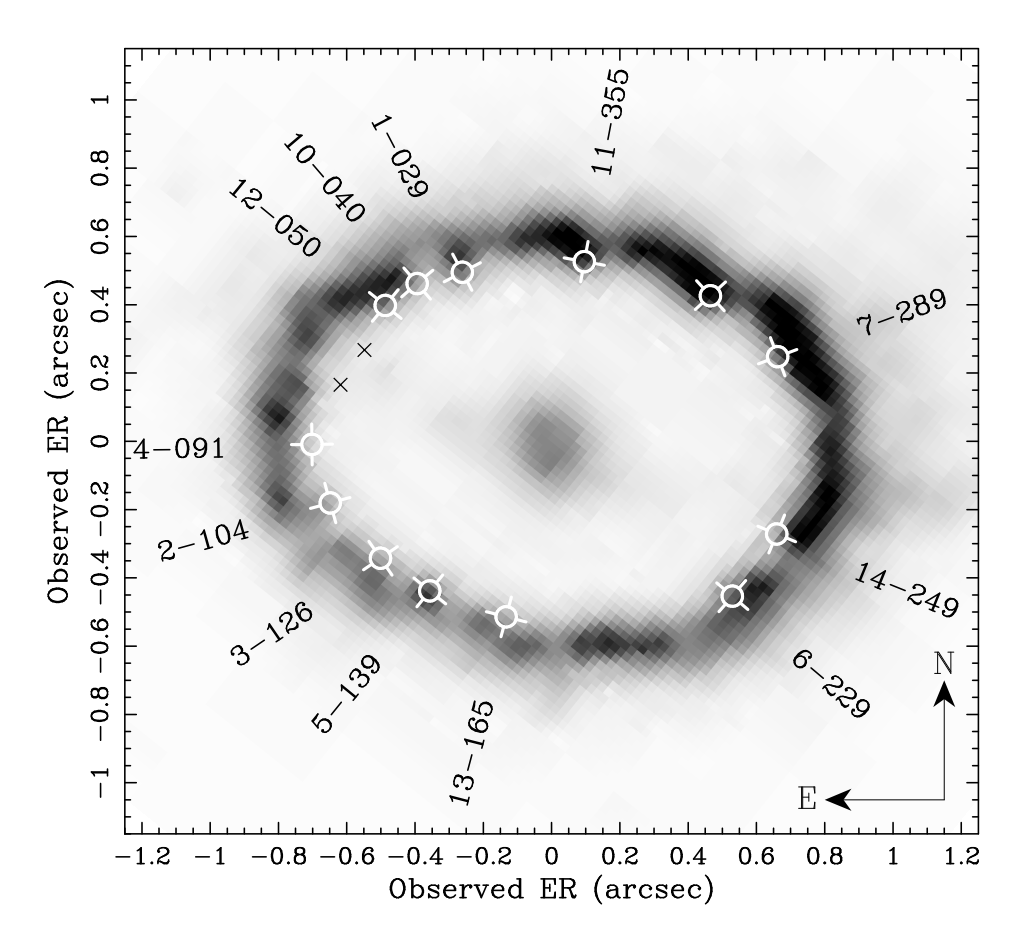


Fig. 4.— WFPC2 F656N image drizzled to double the PC chip resolution (§3.3) with the positions and IDs of hot spots marked. North is up and east is left. Locations of brightening flux attributed to reverse-shocked ejecta are marked with "×". The unlabeled cross-hair near P.A. 314° is a marginally-detected spot (see text).

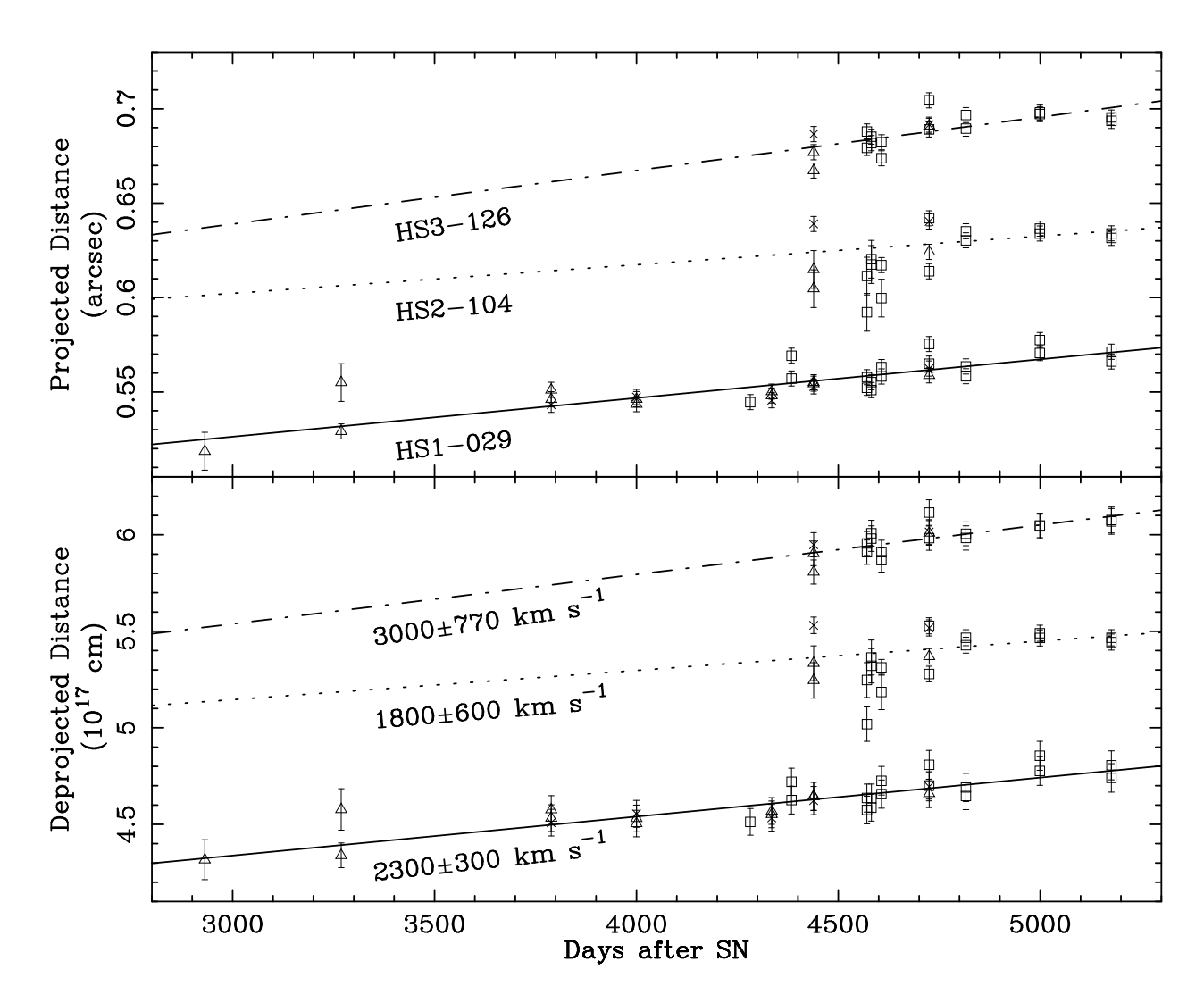


Fig. 5.— Measured distance (top) and deprojected distance (bottom) from the SN of HS 1-029, HS 2-104, and HS 3-126 plotted versus time. Deprojection was performed using the geometric parameters in Table 3. For clarity, the positions of some spots have been shifted vertically: HS 1-029 by  $-0.6 \times 10^{17}$  cm (bottom), HS 2-104 by -0.00 (top), HS 3-126 by 0.00 (top) and  $0.5 \times 10^{17}$  cm (bottom). Centroids were measured using the PSF-fitting algorithms in daophot. Error bars are  $1\sigma$ . STIS F28X50LP data are marked with  $\square$ , WFPC2 F656N data are marked with  $\square$ , and WFPC2 F675W data are marked with  $\square$ . For each spot, the best-fit line (measured via linear least-squares fitting) is drawn through the data: solid lines for HS 1-029, dotted for HS 2-104, and dot-dashed for HS 3-126. The proper motion of the centroid of each hot spot is given by the slope of this line; the resulting velocities in the deprojected frame are listed along each line in the bottom panel, and in Table 2.

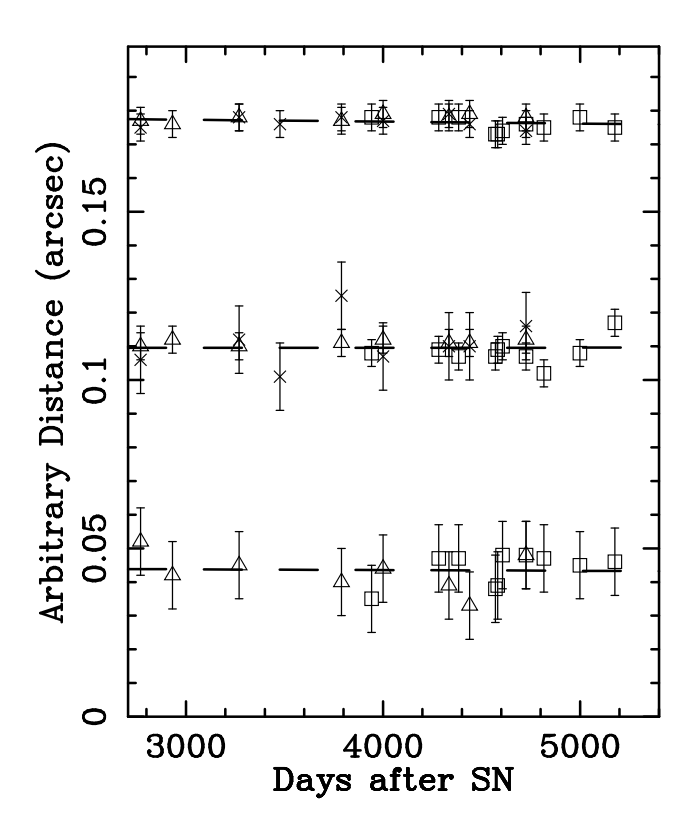


Fig. 6.— Measured distance of three field stars versus time. Symbols are the same as Figure 5. A scalar has been removed from each star's distance to position them such that stellar flux increases with distance. As expected, the positional scatter increases as the flux of the star decreases. Since F656N has a narrower band-pass than the other two filters, the faintest star does not show up in this filter. The best-fit line to each star's data is plotted, and all are consistent with zero proper-motion.

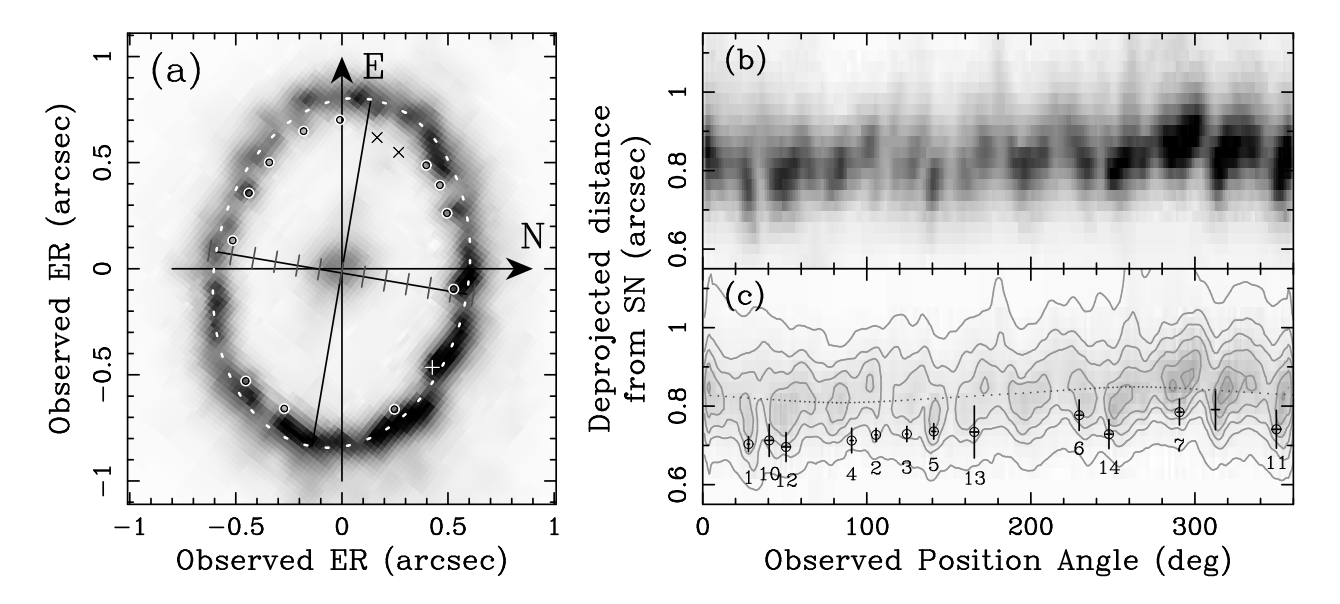


Fig. 7.— (a) High resolution image of the ER from Figure 4 overlayed with the best-fit ellipsoid (dashed white line). Major and minor axes are solid black lines, and light travel delays of one month are marked with gray major ticks along the minor axis. The locations of hot spots are marked by o for confirmed spots and + for the marginal detection. (b) Panel (a) has been radially deprojected using the best-fit ellipsoid axes and orientation, but using the SN centroid, thereby plotting deprojected distance from the SN against observed P.A. (c) The same data as (b) with a lighter colormap and contours to highlight structure. The locations and positional uncertainties of hot spots (Table 1) as well as their IDs are indicated. The dotted line indicates the position of the best-fit ellipse, and appears as a sine wave due to the offset between its centroid and the SN.

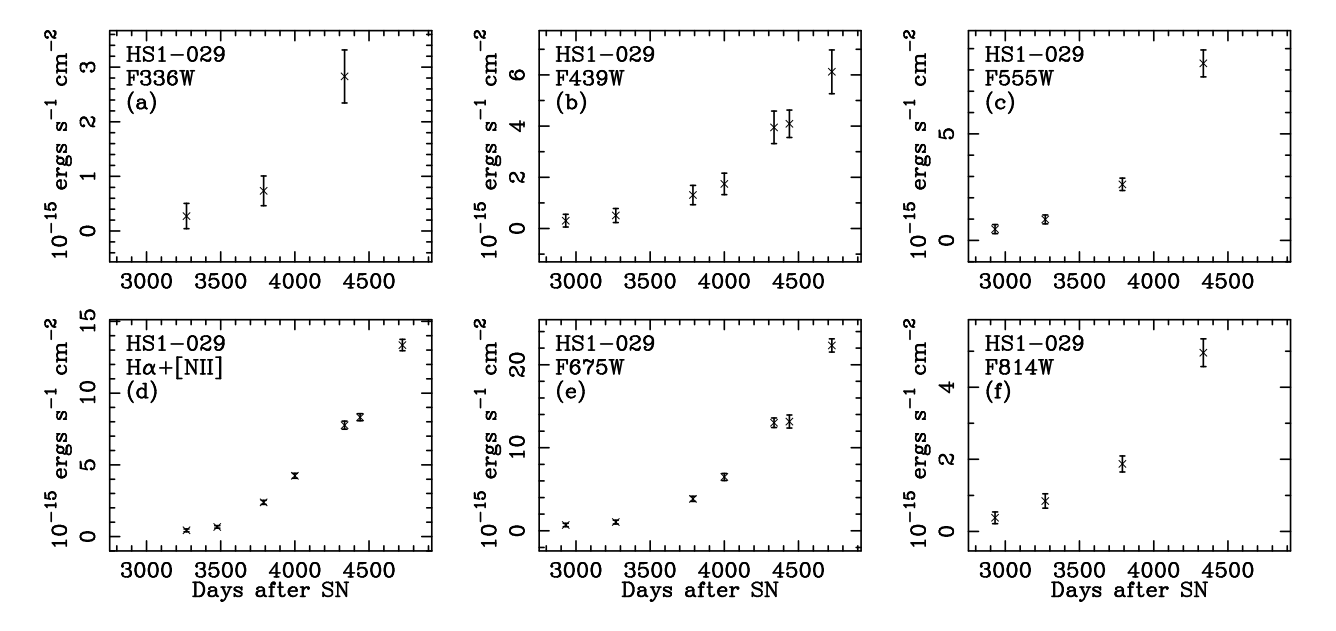


Fig. 8.— Light curves for HS 1-029 in (a) F336W, (b) F439W, (c) F555W, (d) F656N & F658N, (e) F675W, and (f) F814W. Fluxes were measured using the PSF-fitting algorithms in *daophot*. Error bars represent the formally propagated photon-count noise, sky uncertainty and fit errors. Fluxes were calibrated using *symphot*, including decontamination corrections.

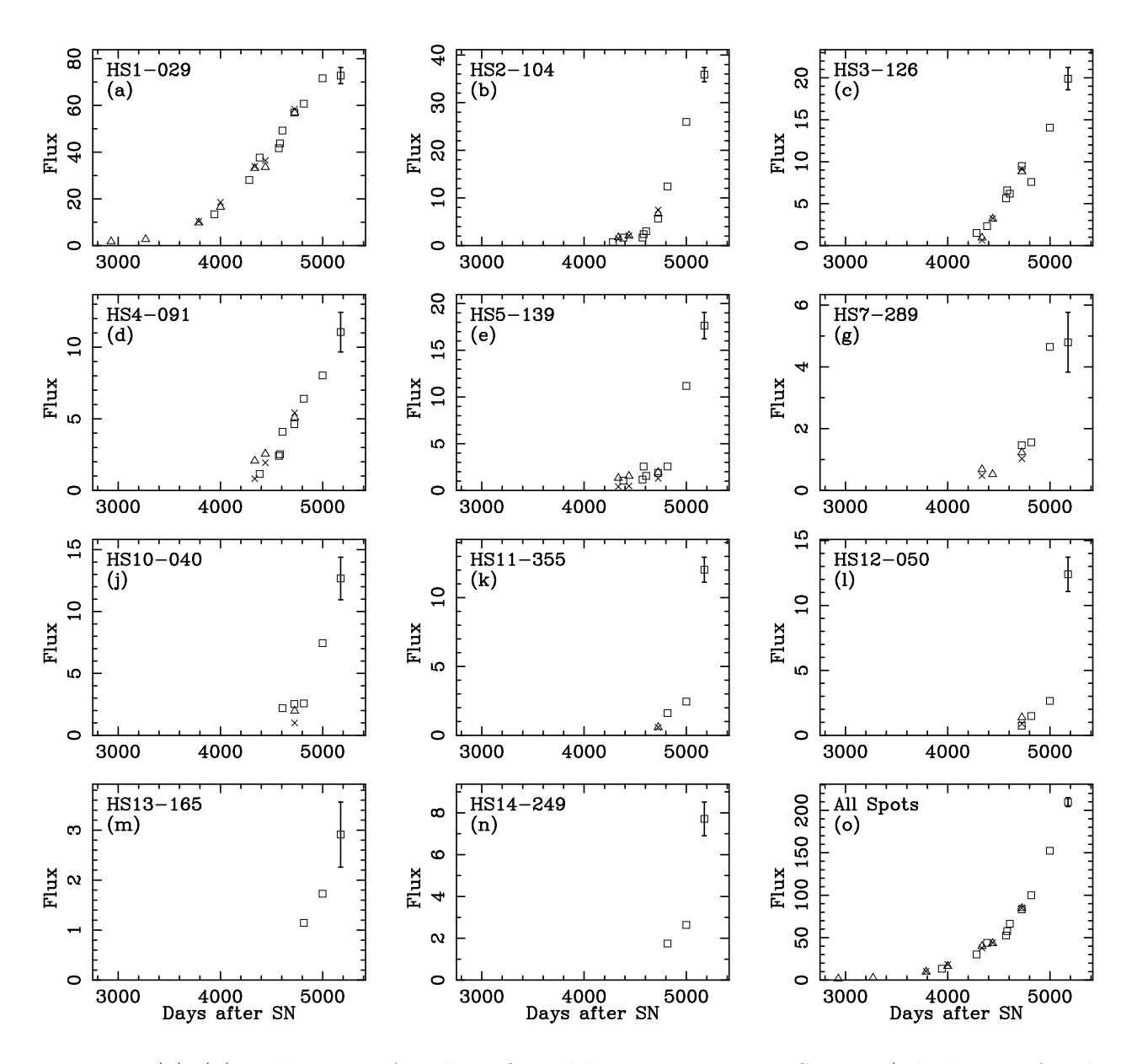


Fig. 9.— (a)–(n) Light curves for all confirmed hot spots except HS 6-229 (which is confused with a coincidentally-aligned star) through HST filters containing  $H\alpha$ . Symbols are the same as Figure 5. Calibrated WFPC2 fluxes have been empirically scaled to native STIS flux (counts  $\sec^{-1}$ ) using HS 1-029 in 2000 February through both imagers:  $F_{\text{F675W}} = 3.92 \times 10^{-16} F_{\text{F28X50LP}}$  and  $F_{\text{F656N}} = 2.29 \times 10^{-16} F_{\text{F28X50LP}}$ . A representational  $1 - \sigma$  error bar has only been plotted on the last point in each panel for clarity. (o) The aggregate light curve of all known hot spot activity by summing the fluxes of each filter over all spots in panels (a)–(n).

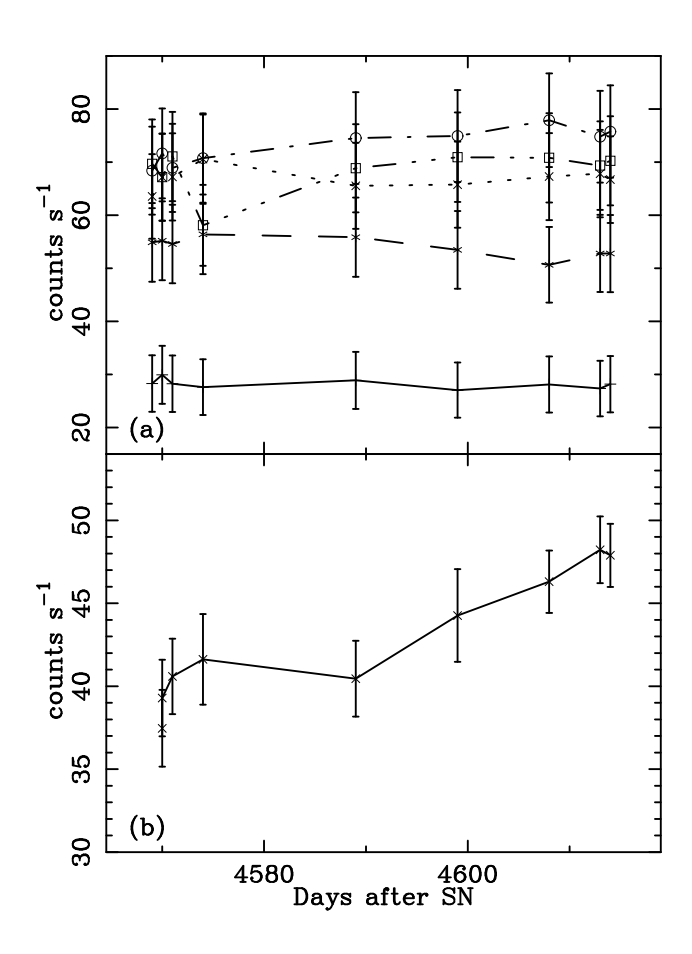


Fig. 10.— (a) Light curves for five stars of flux comparable to HS 1-029 between 1999 August – October through STIS F28X50LP using individual cosmic-ray split pairs of images. We see no evidence for calibration errors between individual epochs. (b) Light curve for HS 1-029 in the same data. The hot spot evolves on timescales of  $\lesssim 1$  month. The rapid variation in the first three points is likely due to bad pixel contamination.

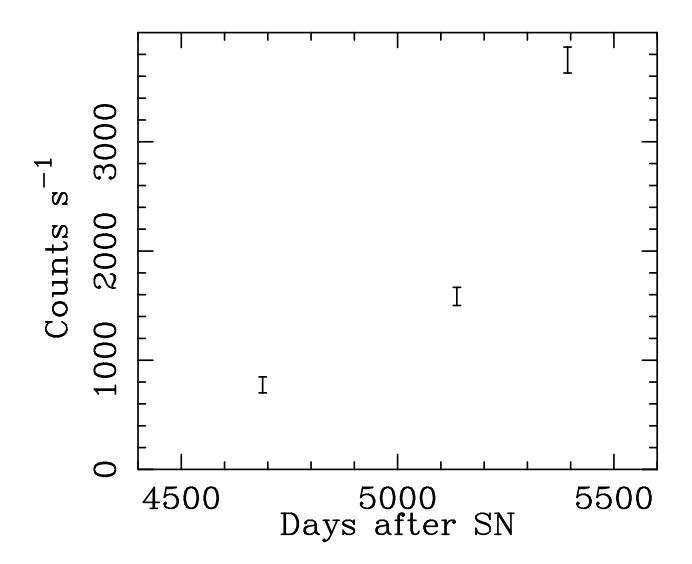


Fig. 11.— Light curve of the increase in He I emission in SNR 1987A since 1998; since HS 1-029 was already a source of line emission at this epoch, this light curve contains an undetermined (but small) zero-point. Data have not been photometrically calibrated, hence we present it in units of instrumental counts per second.

Table 1. Hot Spots in SNR 1987A

	Observed 1	Positions	Deprojected					
Spot	r(")	P.A.(°)	r(")	P.A.(°)	$t_{earliest}^{\mathrm{a}}$	$\Delta t_{light}^{\rm b}$	$v_{blast}^{c}$	$\Delta v_{blast}^{\mathrm{d}}$
HS1-029	$0.560 \pm 0.015$	$27.8 \pm 0.7$	$0.704 \pm 0.019$	$19.3 \pm 0.8$	2933	143	$2590 \pm 940$	843
HS2-104	$0.673 \pm 0.015$	$105.6 \pm 0.7$	$0.727 \pm 0.017$	$113.5 \pm 1.2$	4283	-52	$3347 \pm 496$	544
HS3-126	$0.607 \pm 0.016$	$124.3 \pm 0.6$	$0.729 \pm 0.020$	$133.6 \pm 0.9$	4337	-99	$3546 \pm 582$	574
HS4-091	$0.702 \pm 0.031$	$90.7 \pm 1.1$	$0.712 \pm 0.032$	$94.6 \pm 2.0$	4337	-3	$3215 \pm 903$	500
HS5-139	$0.565 \pm 0.015$	$140.8 \pm 1.2$	$0.736 \pm 0.020$	$148.1 \pm 1.4$	4440	-127	$3908 \pm 578$	613
HS6-229	$0.697 \pm 0.034$	$229.4 \pm 1.8$	$0.777 \pm 0.039$	$220.7 \pm 2.9$	4440	-131	$5108 \pm 1123$	803
HS7-289	$0.707 \pm 0.029$	$290.5 \pm 1.6$	$0.785 \pm 0.033$	$299.2 \pm 2.5$	4440	72	$4992 \pm 896$	722
HS10-040	$0.607 \pm 0.034$	$40.4 \pm 2.3$	$0.713 \pm 0.041$	$31.1 \pm 3.3$	4725	134	$2747 \pm 1005$	350
HS11-355	$0.535 \pm 0.035$	$349.7 \pm 2.9$	$0.741 \pm 0.049$	$349.9 \pm 2.9$	4816	152	$3336\pm1148$	409
HS12-050	$0.629 \pm 0.032$	$50.8 \pm 2.7$	$0.696 \pm 0.037$	$42.2 \pm 4.4$	4816	115	$2292 \pm 887$	285
HS13-165	$0.531 \pm 0.048$	$165.5 \pm 2.4$	$0.734 \pm 0.066$	$166.8 \pm 2.5$	4999	-149	$3281 \pm 1624$	429
HS14-249	$0.713 \pm 0.036$	$247.6 \pm 2.0$	$0.729 \pm 0.037$	$243.0 \pm 3.8$	4999	-79	$3087 \pm 891$	385

<sup>&</sup>lt;sup>a</sup>Earliest detection in *HST* data, days after SN.

<sup>c</sup>Shock velocity, in km s<sup>-1</sup>, required to travel from 0''.6 at day 1300 [the rough epoch and position at which radio emission was first detected, see Manchester et al. (2001)] to a spot given its deprojected position, earliest detection and light-travel delay. For spots 1–3, we use the early-time radial positions shown in Figure 5.

<sup>&</sup>lt;sup>b</sup>Light-travel delay in days, measured from the SN centroid, assuming a distance of 50 kpc.

<sup>&</sup>lt;sup>d</sup>Increase in shock velocity  $v_{blast}$  if a cooling time  $t_c = 1$  yr is included.

 ${\it Table 2.} \quad {\it Least-Squares Fits to Hot Spot Positional Data}$ 

Object	]	Best-Fit Slope				
	Observed $mas yr^{-1}$	Projected <sup>a</sup> km s <sup>-1</sup>	Deprojected <sup>a</sup> km s <sup>-1</sup>			
HS 1-029	$7.49 \pm 0.58$	$1781 \pm 138$	$2338 \pm 300$			
HS 2-104	$5.54 \pm 1.84$	$1315 \pm 437$	$1752 \pm 598$			
HS 3-126	$10.4 \pm 1.5$	$2461 \pm 359$	$2966 \pm 774$			
Field Star 1	$-0.21 \pm 0.39$	$-50 \pm 92$	• • •			
Field Star 2	$0.008 \pm 0.49$	$2 \pm 116$				
Field Star 3	$-0.08 \pm 1.3$	$-19 \pm 310$	•••			

 $<sup>^{\</sup>rm a}{\rm Assuming}$  a distance of 50 kpc.

Table 3. Geometric Parameters of the ER

Parameter	This Work	Plait et a [N II]	l. (1995) [O III]	Burrows et al. (1995)	
Centroid Offset (mas E)	$-20.00 \pm 0.69$	$-13 \pm 44$	$4 \pm 11$	0.	
Centroid Offset (mas N)	$-1.94 \pm 0.36$	$-31 \pm 44$	$7 \pm 11$	0.	
Axial Ratio	$0.722 \pm 0.002$	0.711	0.724	0.711	
Inclination Angle (°)	$43.78 \pm 0.13$	$44 \pm 2$	$43.7\pm1$	44.7	
Semi-Major Axis (")	$0.829 \pm 0.002$	0.845	0.858	0.81	
Semi-Minor Axis (")	$0.599 \pm 0.002$	0.600	0.621	0.57	
P.A. of Major Axis (°E of N)	$80.36 \pm 0.84$	$84.1 \pm 3$	$88.6 \pm 3$	81.2	

Table 4. Detection Reliability and Measurement Accuracy

Flux <sup>a</sup>		Hot Spot Detection			Photometry	Positional Errors (mas)		
$10^{-16} \text{ ergs cm}^{-2} \text{ s}^{-1}$	$N_{ m Detected}$	$N_{ m False}$	$N_{ m Missed}$	% Correct	% Complete	% Error	all star	phot
0.42 - 1.26	14	4	4	60	60			
1.26 - 2.53	12	1	1	91	91	13.5	40.	53.
2.53 - 4.21	10	0	0	100	100	11	29.	22.
4.21 - 42.1	24	0	0	100	100	6.5	8.2	17.

<sup>&</sup>lt;sup>a</sup>These flux bins correspond to  $0.01-0.03,\,0.03-0.06,\,0.06-0.1$  and 0.1-1.0 counts  $\sec^{-1}$  through the F656N filter.

### REFERENCES

Arnett, W.D., Bahcall, J.N., Kirshner, R.P., Woosley, S.E. 1989, ARA&A, 27, 629

Balick, B., Preston, H.L., Icke, V. 1987, AJ, 94, 164

Ball, L., Campbell-Wilson, D., Crawford, D.F., & Turtle, A.J. 1995, ApJ, 453, 864

Borkowski, K.J., Blondin, J.M. & McCray, R. 1997a, ApJ, 476, L31

Borkowski, K.J., Blondin, J.M. & McCray, R. 1997b, ApJ, 477, 281

Bouchet, P., Lawrence, S.S., Crotts, A.P.S., Sugerman, B.E., Uglesich, R.R., & Heathcote, S.R. 2000, IAU Circ., 7354

Burrows, C.J., et al. 1995, ApJ, 452, 680

Burrows, D.N., et al. 2000, ApJ, 543, L149

Chevalier, R.A. 1982, ApJ, 258, 790

Chevalier, R.A., Blondin, J.M., & Emmering, R.T. 1992, ApJ, 392, 118

Chevalier, R.A., & Dwarkadas, V. V. 1995, ApJ, 452, L45

Chevalier, R.A. & Emmering, R.T., 1989, ApJ, 342, L75

Crotts, A.P.S., & Heathcote, S.R. 1991, Nature, 350, 683

Crotts, A.P.S., Kunkel, W.E., & Heathcote, S.R. 1995, ApJ, 438, 724

Crotts, A.P.S., Kunkel, W.E., & McCarthy, P.J. 1989, ApJ, 347, L61

Feast, M. 1999, PASP, 111, 775

Fransson, C., et al. 1989, ApJ, 336, 429

Fruchter, A.S., & Hook, R.N. 1998, PASP, submitted (astro-ph/9808087)

Gaensler, B., Manchester, R., Staveley-Smith, L., Tzioumis, A., Reynolds, J., & Kesteven, M. 1997, ApJ, 479, 845

Garnavich, P., Kirshner, R., & Challis, P. 1997a, IAU Circ., 6710

Garnavich, P., Kirshner, R., & Challis, P. 1997b, IAU Circ., 6761

Garnavich, P., Kirshner, R., & Challis, P. 2000, IAU Circ., 7360

Gould, A. 1994, ApJ, 425, 51

Gould, A., & Uza, O. 1998, ApJ, 494, 118

Holtzman, J., et al. 1995, PASP, 107, 156

Jakobsen, P., et al. 1991, ApJ, 369, L63

Jakobsen, P., Jedrzejewski, R., Macchetto, F., Panagia, N. 1994, ApJ, 435, L47

Jakobsen, P., Macchetto, F., Panagia, N. 1993, ApJ, 403, 736

Kwok, S.O 1982, ApJ, 258, 280

Lawrence, S.S., et al. 2002, in preparation

Lawrence, S.S., & Crotts, A.P.S. 2000, IAU Circ., 7359

Lawrence, S.S., Sugerman, B.E., Bouchet, P., Crotts, A.P.S., Uglesich, R.R., & Heathcote, S.R. 2000, ApJ, 537, 123 (Paper I)

Lawrence, S.S., Sugerman, B.E., & Crotts, A.P.S. 2000, IAU Circ., 7419

Lundvist, P. 1999, ApJ, 511, 389

Lundqvist, P., & Sonneborn, G. 1997, in SN 1987A: Ten Years After, the Fifth CTIO/LCO Workshop, ed. N.B. Suntzeff & M.M. Phillips (San Francisco: ASP), in press (astro-ph/9707144)

Luo, D., & McCray, R. 1991, 379, 659

Luo, D., McCray, R., & Slavin, J. 1994, 430, 246

Manchester, R., et al., astro-ph/0110693, 2001 (accepted by PASA)

Maran, S., Pun, C.S.J., & Sonneborn, G. 2000a, IAU Circ., 7359

Maran, S.P., Sonneborn, G., Pun, C.S.J., Lundqvist, P., Iping, R.C., & Gull, T.R. 2000b, ApJ, 545, 390

Masai, K. & Nomoto, K. 1994, ApJ, 424, 924

Michael, E. 2000, ApJS, 127, 429

Michael, E., McCray, R., Borkowski, K.J., Pun, C.S.J, & Sonneborn, G. 1998, ApJ, 492, L143

Michael, E., et al. 1999, ApJ, 509, L117

Michael, E., et al. 2000, ApJ, 542, L53

Michael, E., et al. 2001, astro-ph/0112261

Panagia, N., Gilmozzi, R., Macchetto, F., Adorf, H.-M., & Kirshner, R. P. 1991, ApJ, 380, L23

Park, S., Burrows, D.N., Garmire, G.P., & Nousek, J.A. 2002, ApJ, In press; astro-ph/0111116

Plait, P., Lundqvist, P., Chevalier, & R., Kirshner, R. 1995, ApJ, 439, 730

Press, W.H., et al. 1992, Numerical Recipes in Fortran 2nd ed. University Press, Cambridge

Pun, C., et al. 1997, IAU Circ., 6665

Reynolds, R., et al. 1995, A&A, 304, 116

Romaniello, M., Salaris, M., Cassisi, S., & Panagia, N. 2000, ApJ, 530, 738

Sonneborn, G., et al. 1998, ApJ, 492, L139

Stavely-Smith, L., et al. 1992, Nature, 355, 147

Stetson, P.B. 1987, PASP, 99, 191

Sugerman, B.E., Lawrence, S.S., & Crotts, A.P.S. 2000, IAU Circ., 7520 (SLC00)

Sugerman, B.E., Lawrence, S.S., & Crotts, A.P.S. 2001a, IAU Circ., 7623

Sugerman, B.E., Lawrence, S.S., & Crotts, A.P.S. 2001b, In "Young Supernova Remnants" Eleventh Astrophysics Conference, College Park, Maryland 2000, American Institute of Physics (New York), eds. S.S. Holt & U. Hwang, p. 129.

Sugerman, B.E., et al. 2002, In preparation

Suzuki, T., Shigeyama, T., & Nomoto, K. 1993, A&A, 274, 883

Tomaney, A., & Crotts, A. P. S. 1996, AJ, 112, 2872

Turtle, A.J., Campbell-Wilson, D., Bunton, J.D., Jauncey, D.L., Kesteven, M.J. 1987, Nature, 327, 38

Wampler, E.J., Richichi, A. 1989, A&A, 217, 31

Wampler, E.J., et al. 1990, ApJ, 362, L13

Wang, L., Mazzali, P.A. 1992, Nature, 355, 58

Woosley, S.E. 1988, ApJ, 330, 218

Xu, J., Crotts, A. P. S., & Kunkel, W. E. 1995, ApJ, 451, 806

This preprint was prepared with the AAS LATEX macros v5.0.